



## ARTICLE

# Tubulin isotypes optimize distinct spindle positioning mechanisms during yeast mitosis

Emmanuel T. Nsamba<sup>1</sup>, Abesh Bera<sup>1</sup>, Michael Costanzo<sup>2</sup>, Charles Boone<sup>2,3,4</sup>, and Mohan L. Gupta Jr.<sup>1</sup>

**Microtubules are dynamic cytoskeleton filaments that are essential for a wide range of cellular processes. They are polymerized from tubulin, a heterodimer of  $\alpha$ - and  $\beta$ -subunits. Most eukaryotic organisms express multiple isotypes of  $\alpha$ - and  $\beta$ -tubulin, yet their functional relevance in any organism remains largely obscure. The two  $\alpha$ -tubulin isotypes in budding yeast, Tub1 and Tub3, are proposed to be functionally interchangeable, yet their individual functions have not been rigorously interrogated. Here, we develop otherwise isogenic yeast strains expressing single tubulin isotypes at levels comparable to total tubulin in WT cells. Using genome-wide screening, we uncover unique interactions between the isotypes and the two major mitotic spindle positioning mechanisms. We further exploit these cells to demonstrate that Tub1 and Tub3 optimize spindle positioning by differentially recruiting key components of the Dyn1- and Kar9-dependent mechanisms, respectively. Our results provide novel mechanistic insights into how tubulin isotypes allow highly conserved microtubules to function in diverse cellular processes.**

## Introduction

Microtubules are essential, dynamic cytoskeletal filaments required for diverse biological processes in eukaryotes, including cell division, intracellular transport, axon formation, and cilia function. They are polymerized from tubulin, a heterodimer of  $\alpha$ - and  $\beta$ -subunits (Nogales, 2000). Microtubules are intrinsically dynamic polymers. A key aspect that allows them to perform diverse processes is that their dynamic behavior can be controlled by a wide range of regulatory proteins (Sturgill and Ohi, 2013; Bodakuntla et al., 2019). The tubulin gene family has undergone evolutionary expansion to produce multiple variants, or isotypes of  $\alpha$ - and  $\beta$ -tubulin that can copolymerize into microtubules in most species (Schatz et al., 1986a; Toda et al., 1984; Gultinan et al., 1987; Krauhs et al., 1981; Theurkauf et al., 1986; Detrich et al., 1987; Little and Seehaus, 1988; Pratt and Cleveland, 1988; Fulton and Simpson, 1976). For example, humans have at least eight  $\alpha$ -isotypes and nine  $\beta$ -isotypes, *Drosophila melanogaster* contains five of each, and the budding and fission yeasts *Saccharomyces cerevisiae* and *Schizosaccharomyces pombe* use one  $\beta$ -isotype and two  $\alpha$ -isotypes. Despite being composed of various isotypes, the canonical structure and dynamic nature of microtubules remain highly conserved. The fundamental question of how cells use multiple tubulin isotypes has remained largely a mystery (Janke and Magiera, 2020).

Determining how cells use tubulin isotypes has been challenging for multiple reasons. Previous studies show isotypes can have distinct influences on the dynamic properties of microtubules (Panda et al., 1994; Honda et al., 2017; Bode et al., 2003), yet obtaining recombinant tubulin from higher eukaryotes for biochemical study was only recently achieved (Minoura et al., 2013; Pamula et al., 2016; Vemu et al., 2016). In cells, excess  $\beta$ -tubulin subunits are toxic (Burke et al., 1989; Weinstein and Solomon, 1990; Katz et al., 1990), while knocking down or removing isotypes can also change the relative ratios of the remaining subunits (Latremoliere et al., 2018). Thus, any isotype-specific effects can be confounded by secondary phenotypes. A limited number of studies in *Drosophila* and *Caenorhabditis elegans* indicate certain isotypes are important for proper spermatogenesis (Hutchens et al., 1997; Hoyle and Raff, 1990), neurite outgrowth (Lockhead et al., 2016; Zheng et al., 2017; Baran et al., 2010), and cilia function (Hurd et al., 2010; Silva et al., 2017), yet the molecular mechanisms remain unclear. Additionally, a range of neurological and reproductive disorders, termed tubulinopathies, results from tubulin mutations (Bahi-Buisson et al., 2014; Feng et al., 2016). The association of certain isotypes with specific disorders suggests they play distinct roles in the cell. Overall, however, a mechanistic understanding of the

<sup>1</sup>Genetics, Development, and Cell Biology, Iowa State University, Ames, IA; <sup>2</sup>Donnelly Centre, University of Toronto, Toronto, Ontario, Canada; <sup>3</sup>Department of Molecular Genetics, University of Toronto, Toronto, Ontario, Canada; <sup>4</sup>Chemical Genomics Research Group, RIKEN Center for Sustainable Resource Sciences, Saitama, Japan.

Correspondence to Mohan L. Gupta Jr.: [mgupta@iastate.edu](mailto:mgupta@iastate.edu).

© 2021 Nsamba et al. This article is distributed under the terms of an Attribution–Noncommercial–Share Alike–No Mirror Sites license for the first six months after the publication date (see <http://www.rupress.org/terms/>). After six months it is available under a Creative Commons License (Attribution–Noncommercial–Share Alike 4.0 International license, as described at <https://creativecommons.org/licenses/by-nc-sa/4.0/>).

contributions of tubulin isotypes to cellular processes, in any organism, is extremely limited.

We used the budding yeast *S. cerevisiae* to investigate how cells use multiple tubulin isotypes. The longstanding paradigm that its two  $\alpha$ -isotypes, *TUB1* and *TUB3*, are functionally interchangeable, is based largely on limited genetic and phenotypic analyses (Richards et al., 2000; Schatz et al., 1986b). While *TUB3* deletion (*tub3* $\Delta$ ) leaves cells viable, loss of *TUB1* is lethal but can be rescued by increased expression of *TUB3* (Schatz et al., 1986b). *tub3* $\Delta$  cells also grow slowly in liquid media and are hypersensitive to the microtubule destabilizer benomyl. Increasing *TUB1* expression overcomes this sensitivity (Schatz et al., 1986b). In Northern blots, *TUB1* appeared to be expressed at higher levels than *TUB3*, but quantitative measurements were not possible due to cross-reactivity of the probes (Schatz et al., 1986a). Together, these data led to the model that Tub1 and Tub3 are functionally interchangeable and their differences result from relatively higher expression of Tub1. This idea is consistent with the observation that tubulin extraction and purification results in mixtures containing more Tub1 than Tub3 (Barnes et al., 1992; Bode et al., 2003) or in immunoblots showing ~30% Tub3 versus 70% Tub1 in cell lysates (Aiken et al., 2019). However, significant differences in aspects of microtubule dynamics between purified Tub1 and Tub3 suggest they may have functional differences (Bode et al., 2003). Because the previous cell-based approaches did not discriminate among the effects of isotype loss, altered overall tubulin levels (Katz et al., 1990), and excess  $\beta$ -subunit toxicity (Burke et al., 1989; Weinstein and Solomon, 1990; Katz et al., 1990), any functional contribution of either isotype has remained elusive.

Using gene replacement, we create otherwise isogenic strains expressing solely *TUB1* or *TUB3* under the regulation of both endogenous loci. They express a single isotype at levels comparable to total  $\alpha$ -tubulin in normal cells. This strategy allows for controlled analyses of the two isotypes that reveal clear functional differences. We uncover genetic connections showing that loss of either isotype uniquely disrupts microtubule functions and that the isotypes display distinct interactions with the two mitotic spindle positioning mechanisms (McNally, 2013). We show that Dynein-dependent spindle positioning is enhanced by Tub1 and compromised by Tub3, whereas the opposite is true for Kar9-dependent positioning. Rather than changes in microtubule dynamics, our data reveal that the increased functionality likely results from selective localization of key components to the microtubule. Using both isotypes results in microtubules that can sufficiently perform the two tasks required for proper spindle positioning. Our findings dispel the paradigm that the yeast tubulin isotypes are functionally interchangeable. Moreover, they uncover a novel role for tubulin isotypes in spindle positioning and provide mechanistic insights into how cells use multiple isotypes to optimize microtubule-dependent functions.

## Results

### Tubulin isotypes in budding yeast are not functionally equivalent

*S. cerevisiae* expresses two  $\alpha$ -tubulin genes, *TUB1* and *TUB3*, and a single  $\beta$ -tubulin, *TUB2* (Schatz et al., 1986a; Neff et al., 1983). The

longstanding paradigm holds that *TUB1* and *TUB3*, along with their gene products, Tub1 and Tub3, are functionally interchangeable, with Tub1 comprising the majority of cellular  $\alpha$ -tubulin. This model rests largely on the observation that *tub3* $\Delta$  cells remain viable, whereas *tub1* $\Delta$  cells, although inviable, can be rescued by increased expression of Tub3 (Fig. 1 a; Richards et al., 2000; Schatz et al., 1986b). To measure Tub1 levels in *tub3* $\Delta$  cells, we used the monoclonal YOL1/34 antibody that was raised against *S. cerevisiae*  $\alpha$ -tubulin (Breitling and Little, 1986). Quantitative immunoblotting showed an ~50% drop in  $\alpha$ -tubulin, indicating Tub3 may constitute approximately half the total  $\alpha$ -tubulin in log-phase cultures (Fig. 1, b and c).

We reasoned that if the isotypes are functionally interchangeable and any differences are simply quantitative, then expressing *TUB1* solely under the regulatory elements of the *TUB3* locus should not support viability. Conversely, expressing *TUB3* from the viability-supporting *TUB1* locus should support viability as the sole source of  $\alpha$ -tubulin. To test this, we replaced the ORF of either *TUB1* or *TUB3* with the other  $\alpha$ -isotype in the context of the local regulatory elements while at the same time deleting that isotype from its endogenous locus (Fig. 1 d). The results show the *TUB1* isotype is sufficient for viability when expressed solely from either the native or *TUB3* locus. The *TUB3* isotype, however, is incapable of supporting viability when solely expressed from either locus (Fig. 1, e and f). This is consistent with each isotype normally composing ~50% of cellular tubulin and shows that regardless of loci, *TUB1* supports essential cellular functions more effectively than *TUB3*. Together, the data are inconsistent with the idea that *TUB1* and *TUB3* are functionally interchangeable and reveal differences that are likely independent of their relative expression.

### Tubulin isotypes display functional differences

Simple deletion of *TUB3* results in sensitivity to the microtubule destabilizer benomyl and reduced spore viability (Schatz et al., 1986b), yet the cytotoxicity and cytoskeletal disruption associated with altered  $\alpha/\beta$ -tubulin stoichiometry and expression levels (Burke et al., 1989; Weinstein and Solomon, 1990; Katz et al., 1990) have limited the characterization of Tub3 loss in these cells. Microtubule characterization in cells lacking the essential *TUB1* has also not been achieved. Thus, how these isotypes contribute to cellular microtubule processes remains unknown.

To determine the functional contributions of *TUB1* and *TUB3*, we generated strains solely expressing either isotype at levels comparable to total  $\alpha$ -tubulin in WT cells. To create cells expressing only *TUB1* (called Tub1 only), we replaced the *TUB3* ORF with that of *TUB1* while seamlessly maintaining the regulatory elements of the endogenous *TUB3* locus (Fig. 2 b). Likewise, to produce cells expressing solely *TUB3* (called Tub3 only), we seamlessly replaced the *TUB1* ORF with that of *TUB3* (Fig. 2 c). Microtubules in Tub1-only or Tub3-only cells are composed exclusively of Tub1 or Tub3, respectively (Fig. 2, a–c). Immunoblotting shows both strains express their respective  $\alpha$ -isotype at levels comparable to total  $\alpha$ -tubulin in control cells (Fig. 2, d and e).

As a first step in evaluating the effects of removing either isotype, we monitored cell growth and sensitivity to carbendazim. In liquid culture, we find replacement of *tub3* $\Delta$  with the

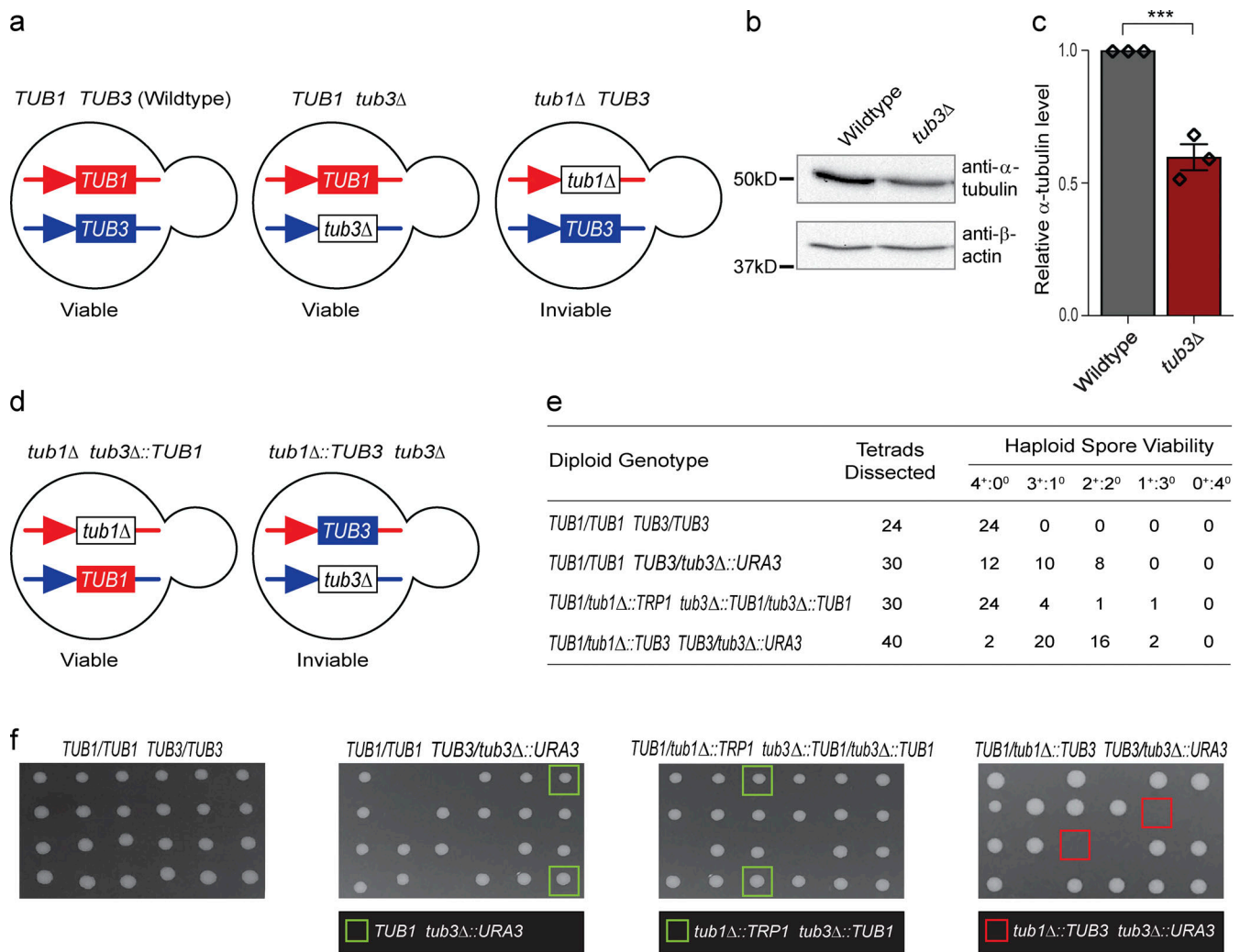


**Figure 1. Tubulin isotypes in budding yeast are not functionally equivalent.** (a) Genetic organization and viability of yeast cells harboring deletions of endogenous  $\alpha$ -tubulin isotypes. (b and c) Representative Western blot (b) and quantification from three independent experiments (c) of  $\alpha$ -tubulin levels in WT and *tub3Δ* cells. Actin is loading control. Mean  $\pm$  SEM; \*\*\*,  $P \leq 0.001$  by unpaired, two-tailed Student's *t* test. Diamonds show individual values from each experiment. (d) Viability of cells with a single  $\alpha$ -isotype gene under regulation of the other isotype locus. (e) Tetrad analyses from diploids with the indicated deletions and substitutions of *TUB1* and *TUB3* genes. +, viable spores; 0, inviable spores. (f) Representative tetrad dissections of strains from panel e. Sister spores are arranged vertically. Green boxes mark representative spores of the indicated genotype to show growth is comparable to sister spores. No haploid spores of *tub1Δ::TUB3 tub3Δ::URA3* genotype were viable (far right). Red boxes mark representative inviable spores that, based on genotype of their surviving sisters, harbor the *tub1Δ::TUB3 tub3Δ::URA3* genotype. As reported, diploids heterozygous for *tub1Δ* or *tub3Δ* also display overall decreased spore viability relative to WT (Schatz et al., 1986b).

*TUB1* ORF (Tub1 only) rescues the slow growth rate previously reported in *tub3Δ* cells (Schatz et al., 1986b). Consequently, both Tub1-only and Tub3-only cells grow in liquid and on agar at rates similar to control cells (Fig. S1, a-d). Strikingly, Tub1-only and Tub3-only cells display opposite sensitivities to carbendazim, which, like benomyl, binds to  $\beta$ -tubulin and destabilizes microtubules (Fig. 2 f; Li et al., 1996). Deletion of *TUB3* (*tub3Δ*) renders cells hypersensitive to benomyl (Schatz et al., 1986b) but also reduces the overall  $\alpha$ -tubulin level (Fig. 1, b and c). This hypersensitivity can be rescued by Tub1 overexpression (Schatz et al., 1986b). Consistent with this, Tub1-only cells, which also lack Tub3 but have  $\alpha$ -tubulin levels comparable to WT, are hyperresistant to carbendazim (Fig. 2 f). Conversely, Tub3-only cells, which lack Tub1 but also possess  $\alpha$ -tubulin levels

comparable to WT, are hypersensitive (Fig. 2 f). This sensitivity is opposite to that predicted from in vitro experiments with purified Tub1- and Tub3-containing heterodimers showing microtubules composed of Tub3 are inherently more stable (Bode et al., 2003). The opposite sensitivities induced by loss of Tub1 or Tub3 reveals that they likely possess distinct functionality.

#### ***TUB1* mRNA level is comparable to *TUB3* in WT cells and unchanged in *tub3Δ* cells**

We used real-time quantitative RT-PCR (RT-qPCR) to further examine isotype expression. RT-qPCR revealed that *TUB1* and *TUB3* mRNA levels are comparable, and each represents  $\sim 50\%$  of total  $\alpha$ -tubulin transcript in WT cultures (Fig. 3 a). In *tub3Δ* cells, we detected no *TUB3* transcript, while the *TUB1* mRNA level

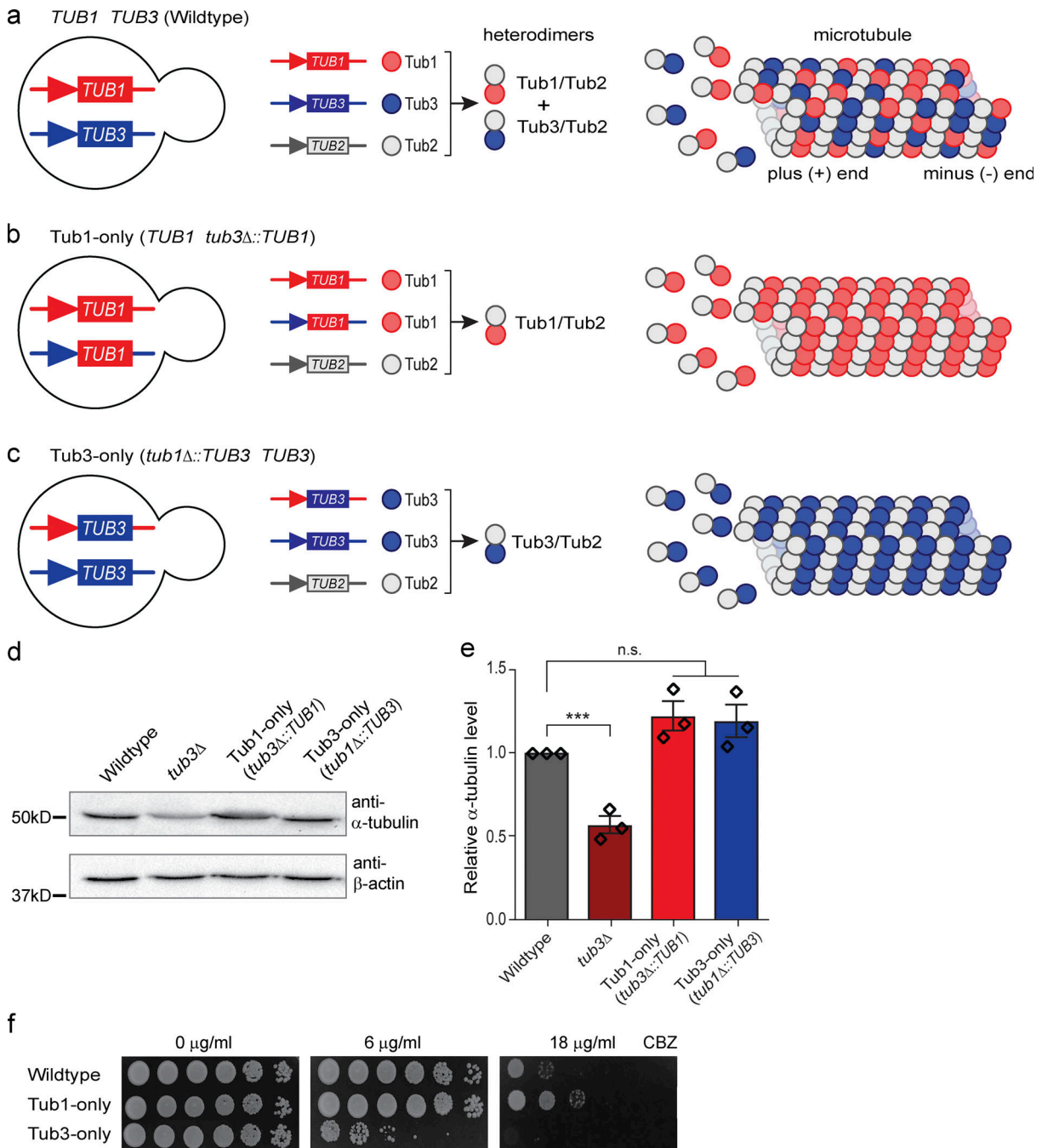
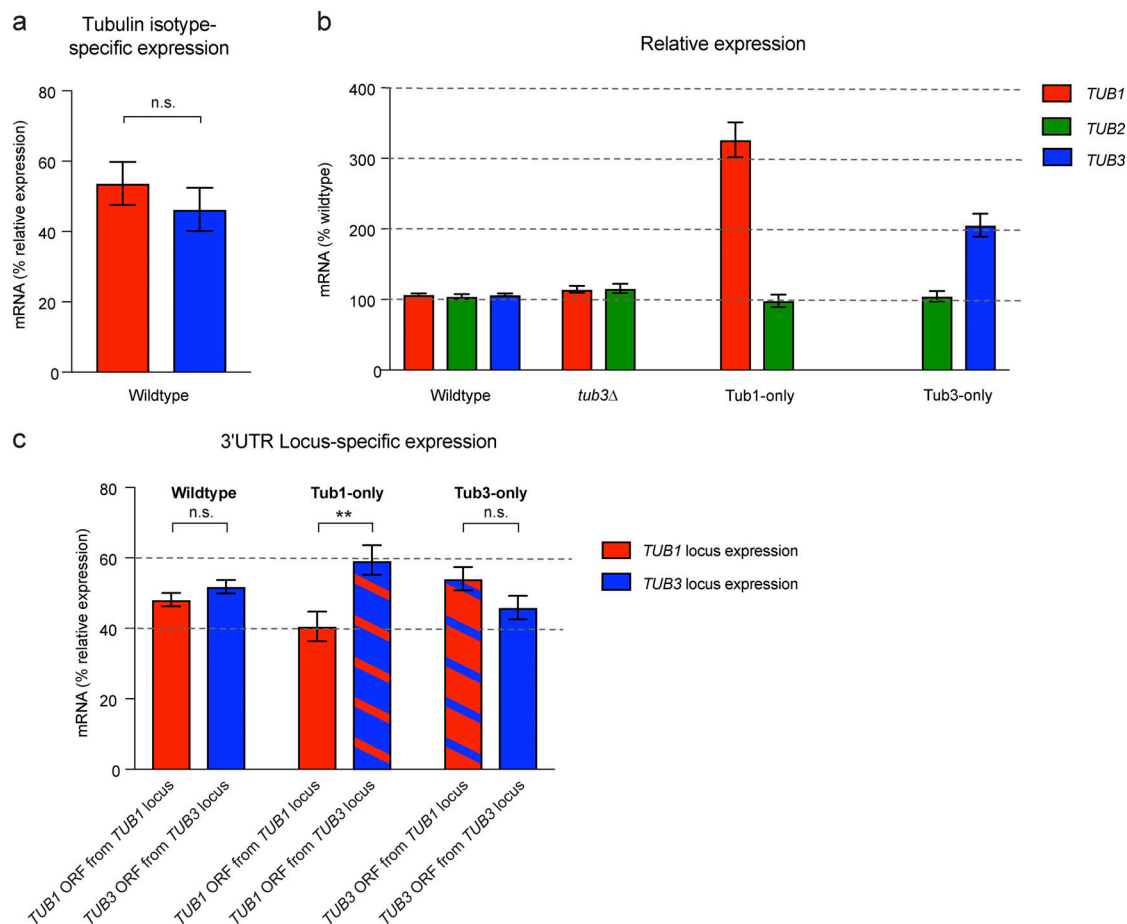


Figure 2. **Tubulin isotypes display functional differences.** (a–c) Genetic organization of WT yeast (a) and those resulting from direct gene replacement to harbor Tub1 only (b) or Tub3 only (c) under endogenous *TUB1* and *TUB3* regulation. For each cell (left), the  $\alpha/\beta$ -heterodimer combinations (center) and composition of cellular microtubules (right) are shown. (d and e) Representative Western blot (d) and quantification from three independent experiments (e) of  $\alpha$ -tubulin levels in the indicated cell types. Actin is loading control. Mean  $\pm$  SEM; \*\*\*,  $P \leq 0.001$  (n.s., not significant, WT vs. Tub1-only and Tub3-only,  $P = 0.13$  and  $0.16$ , respectively) by unpaired, two-tailed Student's *t* test. Diamonds show individual values from each experiment. (f) Carbenzazim (CBZ) sensitivity assay. Serially diluted cultures were spotted onto media with increasing concentrations of the microtubule-destabilizing drug and incubated at 24°C for 3 d.

remained similar to that observed in WT cells (Fig. 3 b). Our immunoblots of *tub3Δ* cells cannot directly report the amount of Tub1 in WT cells, yet the equivalent *TUB1* and *TUB3* transcript levels in WT cells, and the fact that the *TUB1* mRNA level is unchanged in *tub3Δ* cells, are consistent with the observed ~50% drop in  $\alpha$ -tubulin protein in these cells (Fig. 1 c).

*TUB2* mRNA levels remain the same as WT across all genotypes, showing that the  $\alpha$ -tubulin deletion or replacements do not affect  $\beta$ -tubulin expression (Fig. 3 b). In Tub3-only cells, total *TUB3* transcript is increased twofold overexpression solely from the *TUB3* locus in WT cells (Fig. 3 b). In Tub1-only cells, we found the total *TUB1* mRNA level is increased approximately threefold over WT cells (Fig. 3 b). To confirm this finding, we



**Figure 3. *TUB1* mRNA level is comparable to *TUB3* in WT cells and unchanged in *tub3Δ* cells.** (a) *TUB1* (red) and *TUB3* (blue) mRNA levels as a percentage of total expression in WT cells. (b) Transcript levels of *TUB1*, *TUB2*, and *TUB3* in WT, *tub3Δ*, Tub1-only, and Tub3-only cells. (c) 3' UTR-specific transcript levels originating from the *TUB1* locus (red background) or *TUB3* locus (blue background) as a percentage of total expression (cell type is indicated above the bars). For this assay, a forward primer and probe, both with 100% homology to *TUB1* and *TUB3*, were coupled with reverse primers specific to the 3' UTR of either locus. For panels a and b,  $n = 6$  independent cultures and RNA/cDNA preps; for panel c,  $n = 4$  independent cultures and RNA/cDNA preps. In panel b, *TUB1* expression was repeated four times with the redesigned TaqMan assay and twice with the custom assay and the results combined, since expression was similar with either probe/assay. In all panels, graphs show mean  $\pm$  SEM; n.s., not significant; \*\*,  $P \leq 0.01$  by unpaired, two-tailed Student's *t* test.

designed independent RT-qPCR primers and probe, which returned a similar threefold increase (Fig. S1 e). We speculated the excess *TUB1* transcript may result from increased *TUB1* ORF expression when placed in the context of the *TUB3* regulatory elements. To test this, we designed an assay that uses identical sequences in both *TUB1* and *TUB3* for the forward primer and probe and unique reverse primers that are specific to the 3' UTRs of either the *TUB1* or *TUB3* locus. This assay detects transcript originating from each locus regardless of the isotype ORF present. Consistent with the similar *TUB1* and *TUB3* expression seen in WT cells using assays targeting each gene (Fig. 3 a), the 3' UTR-specific assay reveals equivalent mRNA production from both loci in these cells (Fig. 3 c). Likewise, both loci contribute similarly to the twofold increase in *TUB3* transcript in Tub3-only cells (Figs. 3, b and c). In Tub1-only cells, the amount of *TUB1* transcript originating from the *TUB3* locus is 50% higher than that generated by its native locus (Fig. 3 c). It is known that excess *TUB1* gene copies result in excess *TUB1* mRNA, which is selectively down-regulated at the translation and/or protein level (Katz et al., 1990). This is likely how Tub1-only cells,

although possessing excess *TUB1* transcript, harbor Tub1 protein levels similar to total tubulin in WT cells. The mechanism of tubulin homeostasis is poorly defined. Our results suggest proper control of *TUB1*-specific transcript level requires molecular elements within both the ORF and the neighboring regulatory sequences. They also indicate that homeostasis of the Tub1 protein level, compared with transcript, is less sensitive to the *TUB1*- or *TUB3*-specific regulatory elements accompanying the ORF.

Altogether, the data show that under our culture conditions, WT cells express similar levels of Tub1 and Tub3.

#### Mapping genetic interactions of $\alpha$ -tubulin isotypes

Our Tub1-only and Tub3-only strains allowed us to perform synthetic genetic array (SGA) analyses to reveal functional differences between the two  $\alpha$ -isotypes. Most yeast genes have been analyzed by SGA using deletions of nonessential or temperature-sensitive alleles of essential genes to generate a global map of synthetic genetic interactions (Costanzo et al., 2016). However, *tub1Δ* is lethal, and *TUB1* was not included in

the temperature-sensitive alleles. SGA has been performed with *tub3Δ* cells (Costanzo et al., 2016, 2010), but the observed synthetic interactions could arise from the loss of Tub3, the ~50% reduced  $\alpha$ -tubulin level, or possible toxicity from excess  $\beta$ -tubulin subunits (Fig. 1, b and c; Burke et al., 1989; Weinstein and Solomon, 1990; Katz et al., 1990). As a result, the synthetic genetic interactions of either isotype have not been clearly assessed.

The newly inserted isotype ORF segregates with its host locus in Tub1-only and Tub3-only strains (Fig. 2, a-c). Thus, SGA will reveal synthetic interactions between the deletion of a specific gene and the loss of either isotype exclusively. We crossed the single isotype strains to a nonessential deletion library containing ~5,000 genes. Both screens generated ~60 hits that meet the stringent criteria for strong synthetic negative interactions ( $\epsilon$  score < -0.12, P value < 0.05; Table S1). Approximately half the stringent hits were found in both screens, suggesting that some aspects of microtubule function are similarly compromised regardless of which isotype is absent (Fig. 4 a). Alternatively, 35 interactions are specific to loss of Tub1 (Tub3 only) while 34 are unique to loss of Tub3 (Tub1 only; Fig. 4 a). Our results with cells harboring Tub1 at similar levels to normal total  $\alpha$ -tubulin (Tub1 only) also show significant differences with those previously published using *tub3Δ* cells (Costanzo et al., 2016). Of the 59 stringent hits from each screen, only 8 are in common, with 51 genes unique to both the Tub1-only and *tub3Δ* screens (Fig. S2 a). This suggests our screen reports on interactions specific to loss of Tub3 rather than changes in the overall tubulin level or  $\beta$ - to  $\alpha$ -subunit ratio.

The stringent negative interactions identified for the loss of *TUB1* or *TUB3* represent a range of processes based on gene ontology (GO) classification (Fig. 4, b and c; and Fig. S2 b). Both revealed interactions with microtubule-related genes, including motors, spindle elements, tubulin folding cofactors, and components of the spindle assembly checkpoint (Fig. 4 b). The category “chromosome segregation/kinetochore/spindle/microtubule” is the second most populous, representing 4.7- and 3.6-fold enrichment for loss of *TUB1* or *TUB3*, respectively (Fig. 4, b and c). Genes involved in “chromatin/transcription” are hubs on the global genetic interaction network and, as such, are sensitive to perturbations in cellular processes. Indeed, this category represents the largest number of hits, with 7.5- and 4.7-fold enrichment, respectively, for the loss of *TUB1* or *TUB3*, reinforcing that the absence of either isotype perturbs normal microtubule functions (Fig. 4 c). Additional processes, including “drug/ion transport” and “DNA replication/repair,” are also represented (Fig. 4 c). In most categories, over half the interactions are exclusive to the loss of either *TUB1* or *TUB3*. Although some of the differences may be attributable to the false negative and positive rate associated with the SGA screening method (Baryshnikova et al., 2010), overall, these exclusive interactions suggest that microtubule function is uniquely perturbed by loss of either isotype. Altogether, the SGA reveals that Tub1 and Tub3 likely make distinct contributions to a range of microtubule functions.

### Differential roles of $\alpha$ -tubulin isotypes in spindle positioning

Informed by the SGA results showing Tub1 and Tub3 make specific contributions to microtubule function, we explored

their impact on mitotic spindle positioning. Budding yeast undergoes asymmetric cell division in which spindle positioning is a critical microtubule-dependent function. It is executed by two independent and redundant mechanisms (Fig. 4 d; reviewed in McNally, 2013). Early in mitosis, the Kar9-dependent mechanism links astral microtubule plus ends, via a complex of the plus end tracking protein Bim1 (EB1), the APC-related protein Kar9, and the actin motor myosin (Myo2), to polarized actin cables emanating from the bud tip. Myosin-dependent transport of microtubule plus ends to the bud tip positions the pre-anaphase spindle near the bud neck (Fig. 4 d). During anaphase, the Dynein-dependent mechanism pulls the spindle across the bud neck. This is accomplished by Dynein/dynactin together with Bik1 and Kip2 at astral microtubule plus ends interacting with Dynein-activating patches of Num1 on the cell cortex. Dynein movement toward the microtubule minus end pulls the spindle toward the Dynein-Num1 complex (Fig. 4 d). Either mechanism is sufficient to achieve spindle positioning in the absence of the other, but complete loss of both results in spindles remaining within the mother cell. Thus, major components of the Kar9 and Dynein mechanisms display negative synthetic interactions (Miller et al., 1998).

We reasoned if the negative SGA hits for loss of a specific isotype are enriched for genes that themselves display negative synthetic interactions with components of the Kar9 pathway, it suggests that isotype may possess properties important for Kar9 function (Fig. 4 e). Likewise, if the hits preferentially display negative interactions with the Dynein pathway, it indicates that isotype may share functional aspects with the Dynein mechanism (Fig. 4 e). We constructed heatmaps of known synthetic negative interactions between the microtubule-related SGA hits for the loss of either *TUB1* or *TUB3* and major components of the Kar9 and Dynein pathways (Fig. 4 f; Usaj et al., 2017). Remarkably, compared with loss of *TUB3*, the hits from the loss of *TUB1* screen themselves exhibit a 2.5-fold increase in negative interactions, as a proportion of total possible interactions, with Dynein pathway components (Fig. 4, f and g). Albeit to a lesser degree, the hits from the loss of *TUB3* screen show a slightly higher proportion of negative interactions with elements of the Kar9 pathway (Fig. 4, f and g). These distinct genetic interactions suggest Tub1 and Tub3 may play specialized roles in these two microtubule-dependent mechanisms required for cell viability.

### Tub1 optimizes Dynein pathway function

We tested if Tub1 is required for efficient Dynein-mediated spindle positioning. Microtubules are commonly visualized by N-terminal tagging of tubulin with fluorescent proteins (e.g., GFP-Tub1; Luchniak et al., 2013). These constructs are then integrated as an exogenous copy in addition to endogenous *TUB1*. For cells lacking Tub1, we generated an identical construct with the only difference being the *TUB1* ORF replaced with *TUB3* (Fig. 5 a). Thus, microtubules in Tub1-only cells were visualized using GFP-Tub1, and those in Tub3-only using GFP-Tub3. Each construct was introduced separately into WT cells to generate appropriate controls (termed WT-Tub1 and WT-Tub3). Thus, overall, for fluorescent microtubule imaging, Tub1-only cells

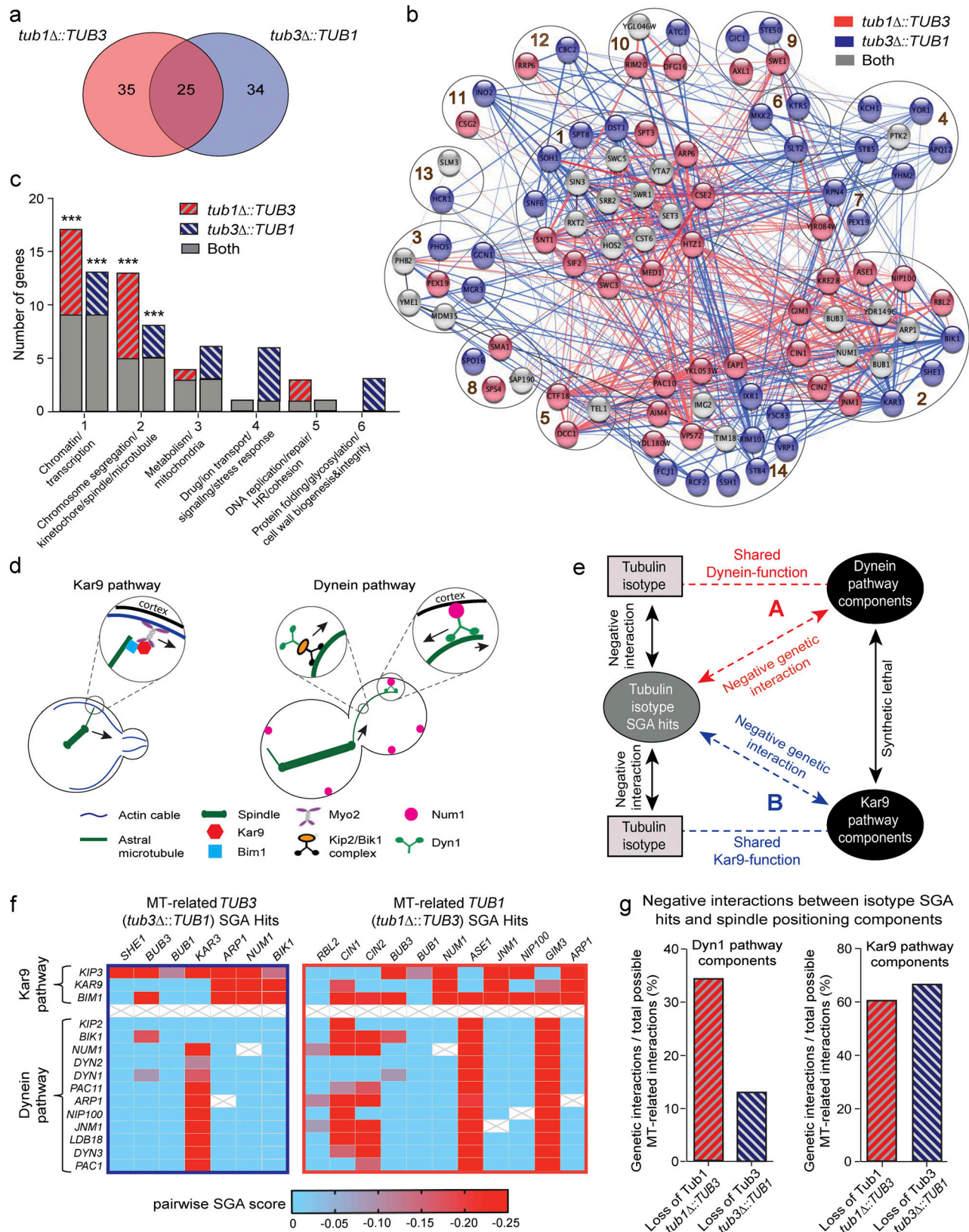


Figure 4. **Mapping genetic interactions of  $\alpha$ -tubulin mutants.** (a) Venn diagram of negative interactions identified in the SGA screens for loss of *TUB1* (red; *tub1Δ::TUB3*) and loss of *TUB3* (blue; *tub3Δ::TUB1*). (b) String network of negative synthetic interactions among the hits from panel a. Genes are clustered by GO terms as follows: 1–6 = depicted in panel c, 7 = protein degradation/proteasome, 8 = cell cycle progression/meiosis, 9 = cell polarity/morphogenesis, 10 = Golgi/endosome/vacuole/sorting, 11 = lipid/sterol/fatty acid biosynthesis, 12 = RNA processing, 13 = ribosome/translation, and 14 = miscellaneous/unknown function. (c) Hits in representative GO-term categories that show negative synthetic interaction with loss of *TUB1* (red hashed; *tub1Δ::TUB3*) or *TUB3* (blue

hashed; *tub3Δ::TUB1*) specifically or both (gray). Significant enrichment marked by \*\*\*,  $P \leq 0.001$  with Fisher's exact test. **(d)** Schematics of Kar9- and Dynein-dependent spindle positioning pathways. In the Kar9 pathway, in early mitosis, Bim1 links microtubule plus ends via Kar9 to the myosin Myo2, which transports the complex toward the bud along polarized actin cables at the cell cortex (McNally, 2013). This "sweeping" of microtubule plus ends moves the associated spindle pole close to the bud neck. In the Dynein pathway, the kinesin Kip2 in complex with Bik1 localizes Dyn1 to microtubule plus ends. Dyn1 together with dynactin (not shown) is activated by contact with Num1 on the cell cortex. Active Dyn1/dynactin "slides" microtubules along the cortex, which pulls the associated spindle pole into the bud (McNally, 2013). **(e)** Model of negative synthetic genetic relationship between hits from the loss of *TUB1* (*tub1Δ::TUB3*) or loss of *TUB3* (*tub3Δ::TUB1*) SGA screens and components of the Kar9 and Dynein pathways. If the SGA hits resulting from the loss of an isotype also display negative synthetic interactions with Dynein pathway components, it indicates that isotype may share functions with the Dynein pathway (A). Negative synthetic interactions between Kar9 pathway components and isotype SGA hits suggest that isotype and the Kar9 pathway may share functions (B). **(f)** Heatmaps of negative synthetic interactions between the microtubule-related genes identified in the loss of *TUB3* (left; *tub3Δ::TUB1*) and loss of *TUB1* (right; *tub1Δ::TUB3*) SGA screens (top row) and components of the Kar9 and Dynein pathways (left column). Each position reports the pairwise synthetic genetic interaction score between the indicated isotype screen hits and Kar9/Dynein pathway components, as previously reported (Usaj et al., 2017). Pairwise score  $< -0.12$  (red) represents strong negative interaction (scale below heatmaps). MT, microtubule. **(g)** Strong negative synthetic interactions between the microtubule-related hits in the loss of *TUB1* (red hashed; *tub1Δ::TUB3*) and loss of *TUB3* (blue hashed; *tub3Δ::TUB1*) and Kar9 or Dynein pathway components as a percentage of total interactions possible from heatmaps in panel f.

exclusively contain Tub1 (in both loci) with an exogenous copy of GFP-Tub1, while Tub3-only cells solely contain Tub3 with an exogenous copy of GFP-Tub3. Correspondingly, the WT-Tub1 and WT-Tub3 controls both harbor native Tub1 and Tub3 with an exogenous copy of GFP-Tub1 or GFP-Tub3, respectively. A similar strategy was used for RUBY3-tagged tubulin (Fig. 5 a; Bajar et al., 2016).

We first investigated the effectiveness of Dynein-mediated spindle positioning (schematic in Fig. 4 d). To isolate the Dynein-dependent mechanism, we used cells lacking *KAR9*. The vast majority of *kar9Δ* cells enter anaphase with a mispositioned spindle and rely on the Dynein pathway for correction (Yin et al., 2000). When cells are dependent on the Dynein pathway, microtubules composed of Tub1 are significantly more efficient at spindle positioning than those made of Tub3 (Fig. 5 b). Both controls are similarly intermediate (Fig. 5 b). Consistent with increased Dynein pathway efficiency, we found that anaphase spindles in Tub1-only cells are better aligned along the mother-bud axis than those in control or Tub3-only cells (Fig. S3 a).

We next examined Dynein-dependent spindle movements, which are predominantly driven by Dynein-mediated sliding of astral microtubules along the cortex (Adames and Cooper, 2000). Microtubule sliding in hydroxyurea (HU)-treated cells arrested in S phase is similar to asynchronously growing cells (Estrem et al., 2017). We synchronized cultures with HU to maximize visualization of sliding events and found the proportion of Tub1-only cells exhibiting Dynein-mediated spindle movements is increased twofold over Tub3-only cells (Fig. 5 c and Video 1). The proportion of control cells displaying Dynein-dependent activity is proportional to their Tub1 gene content (Fig. 5 c). By comparison, cells lacking Dynein (*dyn1Δ*) display no microtubule-dependent sliding events (Fig. S4).

The frequency of Dynein-mediated spindle movement is also increased in Tub1-only relative to Tub3-only cells (Fig. 5 d). Since this is dependent on astral microtubule association with the cortex, we measured the frequency at which microtubule-cortical interactions occur. Microtubules contact the cortex more often in Tub1-only than Tub3-only cells (Fig. 5 e). Notably, when normalized for interaction frequency, the efficiency with which Dynein produces spindle movement is over twofold higher in Tub1-only versus Tub3-only cells, while the efficiency in control cells reflects their exogenous GFP-Tub1 or GFP-Tub3

gene status (Fig. 5 f). Thus, the enhanced Dynein activity in Tub1-only cells is not simply due to increased microtubule-cortex interactions.

Dynein-dependent spindle movements are also more robust in Tub1-only cells. Relative to Tub3-only, spindles are translocated significantly further per event in Tub1-only cells (Fig. 5 g). The duration of these movements is also increased 2.5-fold in Tub1-only over Tub3-only cells (Fig. 5 h). Strikingly, in nearly all parameters measured, Dynein pathway effectiveness is proportional to the *TUB1/TUB3* gene status in the cell (Fig. 5, b–h). Altogether, these data reveal that Tub1 plays a significant role in Dynein-dependent spindle positioning.

#### Tub1 and Tub3 effects on microtubule dynamics cannot explain changes in Dynein activity

Its known increased microtubule stability and/or length can promote longer Dynein-dependent spindle movements (Estrem et al., 2017). Based on this, the increased stability of microtubules made from purified Tub3, relative to Tub1 (Bode et al., 2003), is inconsistent with the more robust Dynein activity in Tub1-only cells (Fig. 5). In contrast to results with purified tubulin (Bode et al., 2003), the relative carbendazim sensitivities of Tub1- and Tub3-only cells suggest Tub1 microtubules may be more stable in vivo, perhaps due to distinct interactions with regulatory proteins or MAPs (Fig. 2 f). This would be consistent with increased Dynein activity in Tub1-only cells. In addition to microtubule dynamics; however, carbendazim sensitivity could also reflect changes in critical microtubule-dependent processes such as kinetochore attachment and spindle midzone function.

To determine if the differences in Dynein-mediated spindle positioning result from changes in microtubule stability, we quantified their dynamics in Tub1- and Tub3-only cells. Dynein more efficiently positions anaphase spindles in Tub1-only cells, yet astral microtubule length during anaphase is indistinguishable in Tub1- and Tub3-only cells (Fig. S3 b). In HU-treated cells, microtubule length at the start of Dynein-mediated movement is slightly longer in Tub1-only and WT-Tub1 cells, but the lengths are not proportional to the *TUB1/TUB3* ratio, as seen with nearly all parameters of Dynein activity (Fig. 5 i). We also monitored dynamic instability of individual microtubules (Fig. S5 and Videos 2, 3, and 4). Although polymerization and depolymerization rates are increased in HU-treated relative to nontreated



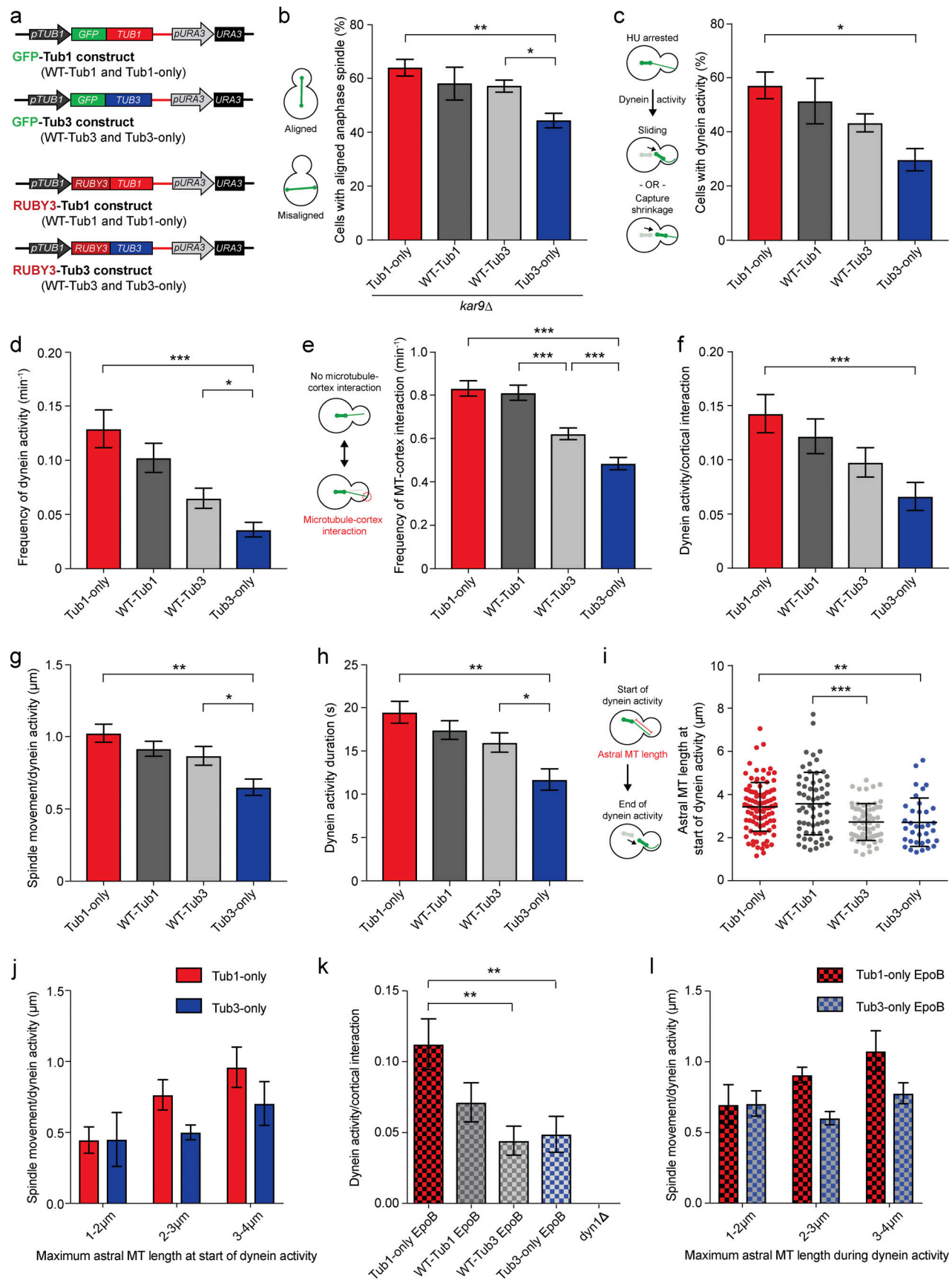


Figure 5. **Tub1 optimizes Dyn1 pathway function.** (a) Schematics of GFP- and mRUBY3-tubulin fusion constructs used to visualize microtubules in the indicated single isotype and control cells. (b) Percentage of *kar9Δ* cells with the indicated tubulin isotypes that display properly aligned anaphase spindles.

**(c)** Percentage of cells displaying Dynein-mediated spindle movements during 10-min observation. **(d)** Frequency of Dynein-mediated spindle movements in individual cells. **(e)** Frequency of astral microtubule contact with the bud cell cortex in individual cells. **(f)** Dynein-mediated spindle movements normalized by microtubule–cortex interactions in individual cells. **(g)** Spindle translocation per Dynein-mediated event. **(h)** Duration of Dynein-mediated spindle movements. **(i)** Astral microtubule length at initiation of Dynein-mediated spindle movements. **(j)** Spindle translocation per Dynein-mediated event binned by astral microtubule length. **(k)** Dynein-mediated spindle movements normalized by microtubule–cortex interactions in epothilone B (EpoB)-treated cells. **(l)** Spindle translocation per Dynein-mediated event binned by astral microtubule length in EpoB-treated cells. For panels b and c, graphs show mean  $\pm$  SEM from three trials. In panel b, for Tub1 only,  $n = 86, 92,$  and  $150$ ; for WT-Tub1,  $n = 83, 107,$  and  $117$ ; for WT-Tub3,  $n = 98, 76,$  and  $163$ ; for Tub3 only,  $n = 66, 113,$  and  $158$ . In panel c,  $n = 40, 30,$  and  $30$  cells for each genotype. For panels d–i, graphs show mean  $\pm$  SEM from 90–100 cells observed over three trials, where  $n = 40, 20–30,$  and  $30$  for each genotype. For panels g–i, the total number of events recorded is 128, 92, 65, and 36 for Tub1 only, WT-Tub1, WT-Tub3, and Tub3 only, respectively. In panels j–l, graphs show mean  $\pm$  SEM; panel j includes a total of 33 and 10 Dynein events from three trials for Tub1-only and Tub3-only cells, and panel l includes a total of 56 and 22 Dynein events from two trials for Tub1-only and Tub3-only cells, respectively; for panel k,  $n = 40, 30, 30,$  and  $40$  cells analyzed from two trials for Tub1 only, WT-Tub1, WT-Tub3, and Tub3 only, respectively. \*,  $P \leq 0.05$ ; \*\*,  $P \leq 0.01$ ; and \*\*\*,  $P \leq 0.001$  by unpaired, two-tailed Student's  $t$  test. MT, microtubule.

preanaphase cells, the major difference is a shorter polymerization duration and slower depolymerization rate for Tub3-only relative to Tub1-only microtubules (Table 1). Despite microtubules in Tub3-only cells having  $\sim 40\%$  reduced polymerization duration and overall 9.3% reduction in time spent polymerizing compared with Tub1-only, this is partly offset by their 5.3% increase in time attenuated (Table 1). Also, in lifetime history plots of Tub1-only microtubules, 77% of polymerizations were followed by depolymerization (catastrophe) rather than attenuation, whereas with Tub3-only microtubules, this drops to 66%. Together, these effects likely contribute to the similar catastrophe frequency seen in Tub1- and Tub3-only cells. Overall, microtubules in Tub3-only cells have somewhat reduced dynamicity compared with Tub1-only (Table 1). Dynein activity is correlated with increased microtubule stability (Estrem et al., 2017). Thus, a similar catastrophe frequency yet significantly slower depolymerization for Tub3- relative to Tub1-only microtubules indicate that increased microtubule stability does not likely underlie the robust Dynein activity in Tub1-only cells.

To further examine the role of microtubule length and stability in isotype-specific Dynein function, we compared spindle

movement as a function of microtubule length. When binned by length, longer Tub1-only microtubules support larger Dynein-dependent translocations than Tub3-only microtubules of comparable lengths (Fig. 5 j). We next treated cells with the microtubule-stabilizing compound epothilone. Although in our hands, epothilone treatment does not produce substantially longer microtubules during Dynein-mediated events (Fig. S4 a; Estrem et al., 2017), it does significantly stabilize astral microtubules (Fig. S5 and Videos 5 and 6). Overall, during epothilone treatment, the proportion of cells displaying Dynein activity remains elevated in Tub1-only and decreased in Tub3-only (Fig. S4 b). The frequency of Dynein activity, as well as spindle movement per event, is also highly elevated in epothilone-treated Tub1- versus Tub3-only cells (Fig. S4, c and e). When normalized for cortical interactions, the frequency of Dynein activity in epothilone-treated cells is  $\sim 2.5$ -fold higher in Tub1-only compared with Tub3-only cells (Fig. 5 k). When epothilone-stabilized microtubules are binned by maximum length during sliding, Tub1-only microtubules continue to support larger spindle translocations than Tub3-only microtubules of similar lengths (Fig. 5 l). Together, these data support the conclusion

Table 1. Parameters of dynamic instability for astral microtubules in HU-arrested cells

	Tub1 only	WT-Tub1	WT-Tub3	Tub3 only
Polymerization rate ( $\mu\text{m}/\text{min}$ )	2.11 $\pm$ 0.11 (52)	2.18 $\pm$ 0.08 (77)	2.17 $\pm$ 0.13 (55)	2.11 $\pm$ 0.08 (66)
Depolymerization rate ( $\mu\text{m}/\text{min}$ )	5.17 $\pm$ 0.21 (53)	4.74 $\pm$ 0.18 (72)	4.79 $\pm$ 0.02 (61)	3.83 $\pm$ 0.13 (57) <sup>a</sup>
Catastrophe frequency ( $\text{min}^{-1}$ )	0.97 (46)	0.96 (65)	1.06 (51)	1.02 (49)
Rescue frequency ( $\text{min}^{-1}$ )	0.12 (3)	0.39 (15)	0.10 (3)	0.13 (4)
Polymerization duration, s	50.4 $\pm$ 4 (52)	49.2 $\pm$ 3 (77)	50.3 $\pm$ 4 (55)	31.8 $\pm$ 2 (66) <sup>b</sup>
Depolymerization duration, s	28.3 $\pm$ 2 (53)	32.0 $\pm$ 1 (72)	30.0 $\pm$ 1 (61)	36.3 $\pm$ 2 (57)
Dynamicity, tubulin/s	86.28	84.70	88.16	71.96
Time spent polymerizing, %	60.39	59.37	58.64	51.06
Time spent depolymerizing, %	34.63	36.16	38.73	38.63
Time spent attenuated, %	4.98	4.47	2.63	10.31
Total microtubules observed	52	57	58	54
Total time observed, s	4,337	6,375	4,720	4,693

Results are presented as mean  $\pm$  SEM, with sample number shown in parentheses.

<sup>a</sup> $P \leq 0.001$  versus Tub1 only, WT-Tub 1, and WT-Tub3 by unpaired, two-tailed Student's  $t$  test.

<sup>b</sup> $P \leq 0.01$  versus Tub1 only and WT-Tub3;  $P \leq 0.001$  versus WT-Tub1 by unpaired, two-tailed Student's  $t$  test.

that differences in microtubule length or stability do not likely underlie the robust Dynein function in Tub1-only or the diminished activity in Tub3-only cells.

### Tub1 preferentially directs Dynein pathway proteins to astral microtubule plus ends

The observed changes in Dynein function are not correlated with altered microtubule dynamics, suggesting isotype-specific perturbation of Dynein pathway proteins. We quantified the localization of Dynein (Dyn1 in yeast) and related proteins by fluorescent tagging at their endogenous loci. In control cells, Dyn1-3GFP localizes prominently to astral microtubule plus ends, spindle pole bodies (SPBs) and cortical-associated foci in the mother and bud (Fig. 6 a). Strikingly, the amount of Dyn1-GFP localized to plus ends of Tub1-only microtubules is nearly 2.5-fold that seen with Tub3-only (Fig. 6 b). The proportion of Tub1-containing cells that display visible Dyn1-GFP foci at microtubule ends is also increased by 50% (Fig. 6 c). While the intensity of Dyn1-GFP foci on the bud cortex is slightly decreased in Tub3-only cells, their brightness at the mother cortex is more than doubled compared with Tub1-only cells (Figs. 6 d and S3 c). The intensity of Dyn1-GFP foci at the SPB is comparable in Tub1- and Tub3-only cells (Fig. S3 d).

Similar to Dyn1, the localization of Bik1 and Kip2 is enhanced in Tub1-only and diminished in Tub3-only cells. While the proportion of cells with Bik1-3GFP foci at microtubule ends is slightly increased in Tub1-only cells (Fig. S3 e), the intensity of those foci is ~2.5-fold higher relative to Tub3-only cells (Fig. 6 e). Tub1-only microtubules also have more Bik1-3GFP foci along their length than those in Tub3-only cells (Fig. 6 f). Consistent with its role of transporting Bik1 (Carvalho et al., 2004), Kip2-3YFP levels are significantly elevated at microtubule plus ends in Tub1-only compared with Tub3-only cells (Fig. 6 g).

Altogether, these data show that compared with control cells, microtubules in Tub1-only cells, lacking Tub3, facilitate increased localization of critical Dynein pathway components. Conversely, the absence of Tub1 results in diminished localization in Tub3-only cells. This localization is directly correlated with the function of the Dynein-mediated pathway, which is enhanced in Tub1-only cells relative to controls and significantly impaired in Tub3-only cells.

### Tub3 optimizes spindle positioning by the Kar9 pathway

Our genetic analysis revealed that Tub1 functions preferentially in the Dynein-mediated mechanism and suggests Tub3 may perhaps operate similarly in the Kar9 pathway. To test this, we examined the efficiency of Kar9-mediated spindle positioning (schematic in Fig. 4 d). In small-budded Tub3-only cells, pre-anaphase spindles are properly positioned near the bud neck slightly more efficiently than in control cells (Fig. 7 a). By contrast, positioning is significantly impaired in cells lacking Tub3. In Tub1-only cells, the effectiveness of the Kar9 pathway is midway between fully functional Tub3-containing controls and completely null *kar9Δ* cells (Fig. 7 a). The same trend is reflected in spindle distance from the bud neck (Fig. 7 b). Kar9-dependent positioning is achieved by myosin-directed sweeping of astral microtubules along the mother cortex to the bud. In control

cultures, the vast majority of small-budded cells have a microtubule oriented toward the bud (Fig. 7 c). A similar proportion is seen in Tub3-only cultures (Fig. 7 c). By comparison, Tub1-only cultures, which lack Tub3, have significantly fewer cells with bud-oriented astral microtubules (Fig. 7 c).

To test if the effect on Kar9 function is strictly due to isotype composition and not influenced by the GFP-Tub1 or GFP-Tub3 used to visualize microtubules in the single isotype strains and their respective controls, we alternatively visualized SPBs using endogenously tagged Cnm67-RUBY2. This provided a control cell with truly WT tubulin isotype composition (*TUB1 TUB3*), along with Tub1-only (*TUB1 TUB1*) and Tub3-only (*TUB3 TUB3*) cells without exogenously tagged GFP-tubulin. Notably, by monitoring Kar9-dependent positioning in these cells, we obtained results equivalent to those using GFP-tagged tubulin (Fig. S6).

Together, these data show that Kar9-mediated spindle positioning is substantially impaired by the loss of Tub3, yet in the absence of Tub1, Tub3 alone supports optimal functioning of the Kar9 pathway.

### Tub3 preferentially directs Kar9 pathway proteins to astral microtubule plus ends

To elucidate the molecular basis for Tub3 efficiency in the Kar9 pathway, we first determined if astral microtubule length is correlated with spindle positioning. Although the average length is reduced in small-budded Tub3-only cells, the lengths are comparable between Tub1-only and the controls WT-Tub1 and WT-Tub3 (Fig. 7 d). In contrast, Kar9-dependent positioning is significantly impaired in Tub1-only cells compared with Tub3-only and controls, which harbor Tub3 as well (Fig. 7, a and b; and Fig. S6). Positioning is also somewhat increased in Tub3-only cells relative to controls (Fig. 7, a and b). Likewise, Kar9-mediated microtubule transport to the bud is specifically perturbed in Tub1-only cells relative to Tub3-only and the controls (Fig. 7 c). Astral microtubule length, therefore, is not correlated with spindle positioning. Thus, changes in microtubule dynamics are likely not responsible for the isotype-specific differences in Kar9 pathway function.

We next quantified the localization of Kar9 pathway components. Bim1 localizes to plus ends and links Kar9 to microtubules (Lee et al., 2000). In small-budded cells with nascent spindles, comparable proportions of Tub1-only, Tub3-only, and both controls display Bim1 foci at the plus ends of bud-directed microtubules (Fig. 8 a). The amount of Bim1 at the end, however, is significantly decreased in Tub1-only compared with Tub3-only cells (Fig. 8 b). Bim1 localization in Tub3-only cells is also enhanced relative to control cells that contain a mixture of Tub1 and Tub3 (Fig. 8 b). The proportion of bud-directed microtubules with plus end foci of Kar9 is slightly reduced in Tub1-only compared with Tub3-only cells (Fig. 8 c). Moreover, the quantity of Kar9 localized to plus ends is significantly reduced in Tub1-only relative to Tub3-only cells (Fig. 8 d). Altogether, these results suggest that reduced Bim1 and Kar9 recruitment in the absence of Tub3 may result in defective Kar9 pathway function.

We hypothesized that if Tub3 normally functions to recruit sufficient Bim1-Kar9 for early spindle positioning, restoring plus end localization in the absence of Tub3 would rescue the

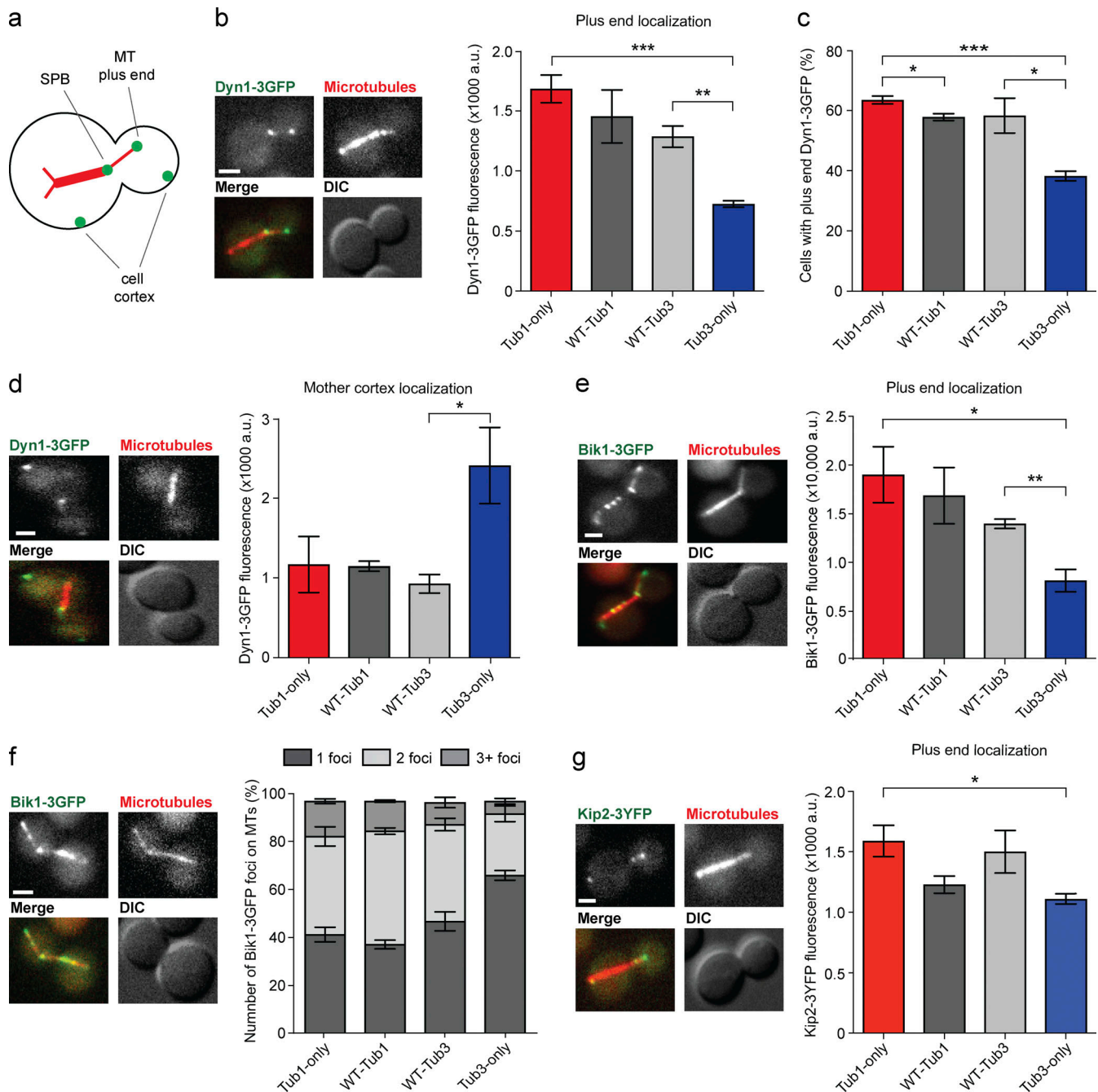


**Figure 6. Tub1 preferentially directs Dynein pathway proteins to astral microtubule plus ends.** (a) Schematic of Dyn1-3GFP localization (green) in WT cells. (b) Dyn1-3GFP localization to microtubule plus ends. Left: Representative wide-field and DIC images showing Dyn1-3GFP localization to SPB and astral microtubule plus end. Right: Dyn1-3GFP signal at microtubule plus ends. (c) Percentage of cells with visible Dyn1-3GFP foci at astral microtubule plus ends. (d) Dyn1-3GFP localization to mother cell cortex. Left: Cell images showing Dyn1-3GFP localization at mother cortex. Right: Dyn1-3GFP signal at mother cortex foci. (e) Bik1 localization to microtubule plus ends. Left: Cell images showing Bik1-3GFP localization to the spindle, SPBs and astral microtubule plus ends. Right: Bik1-3GFP signal at microtubule plus ends. (f) Bik1 localization along astral microtubules. Left: Cell images showing Bik1-3GFP localization along astral microtubules. Right: Number of Bik1-3GFP foci along bud-directed astral microtubules. For Tub1 only versus Tub3 only,  $P = 0.002$ ,  $0.04$ , and  $0.004$  for one, two, and three or more foci; for Tub3 only versus WT-Tub3,  $P = 0.012$  and  $0.024$  for one and two foci, respectively. (g) Kip2 localization to microtubule plus ends. Left: Cell images showing Kip2-3YFP localization along and at plus ends of astral microtubules. Right: Kip2-3YFP signal at microtubule plus ends. For panels b–g, microtubules are visualized by mRUBY3-Tub1 or mRUBY3-Tub3; merge shows microtubules in red and GFP-tagged proteins in green. Graphs show mean  $\pm$  SEM from three trials. In panel b, for Tub1 only,  $n = 47$ ,  $58$ , and  $60$ ; for WT-Tub1,  $n = 54$ ,  $57$ , and  $70$ ; for WT-Tub3,  $n = 54$ ,  $68$ , and  $52$ ; for Tub3 only,  $n = 61$ ,  $60$ , and  $51$ . In panel c, for Tub1 only,  $n = 69$ ,  $59$ , and  $58$ ; for WT-Tub1,  $n = 82$ ,  $55$ , and  $61$ ; for WT-Tub3,  $n = 63$ ,  $60$ , and  $87$ ; for Tub3 only,  $n = 53$ ,  $63$ , and  $85$ . In panel d, for Tub1 only,  $n = 26$ ,  $48$ , and  $42$ ; for WT-Tub1,  $n = 38$ ,  $25$ , and  $21$ ; for WT-Tub3,  $n = 40$ ,  $54$ , and  $54$ ; for Tub3 only,  $n = 55$ ,  $42$ , and  $25$ . In panel e, for Tub1 only,  $n = 49$ ,  $58$ , and  $57$ ; for WT-Tub1,  $n = 56$ ,  $50$ , and  $60$ ; for WT-Tub3,  $n = 56$ ,  $62$ , and  $60$ ; for Tub3 only,  $n = 50$ ,  $61$ , and  $55$ . In panel f, for Tub1 only,  $n = 65$ ,  $62$ , and  $63$ ; for WT-Tub1,  $n = 76$ ,  $73$ , and  $61$ ; for WT-Tub3,  $n = 67$ ,  $63$ , and  $70$ ; for Tub3 only,  $n = 68$ ,  $63$ , and  $81$ . In panel g, for Tub1 only,  $n = 59$ ,  $60$ , and  $60$ ; for WT-Tub1,  $n = 60$ ,  $60$ , and  $67$ ; for WT-Tub3,  $n = 60$ ,  $60$ , and  $60$ ; for Tub3 only,  $n = 63$ ,  $60$ , and  $60$ . \*,  $P \leq 0.05$ ; \*\*,  $P \leq 0.01$ ; \*\*\*,  $P \leq 0.001$  by unpaired, two-tailed Student's *t* test. Scale bars =  $2 \mu\text{m}$ . MT, microtubule.

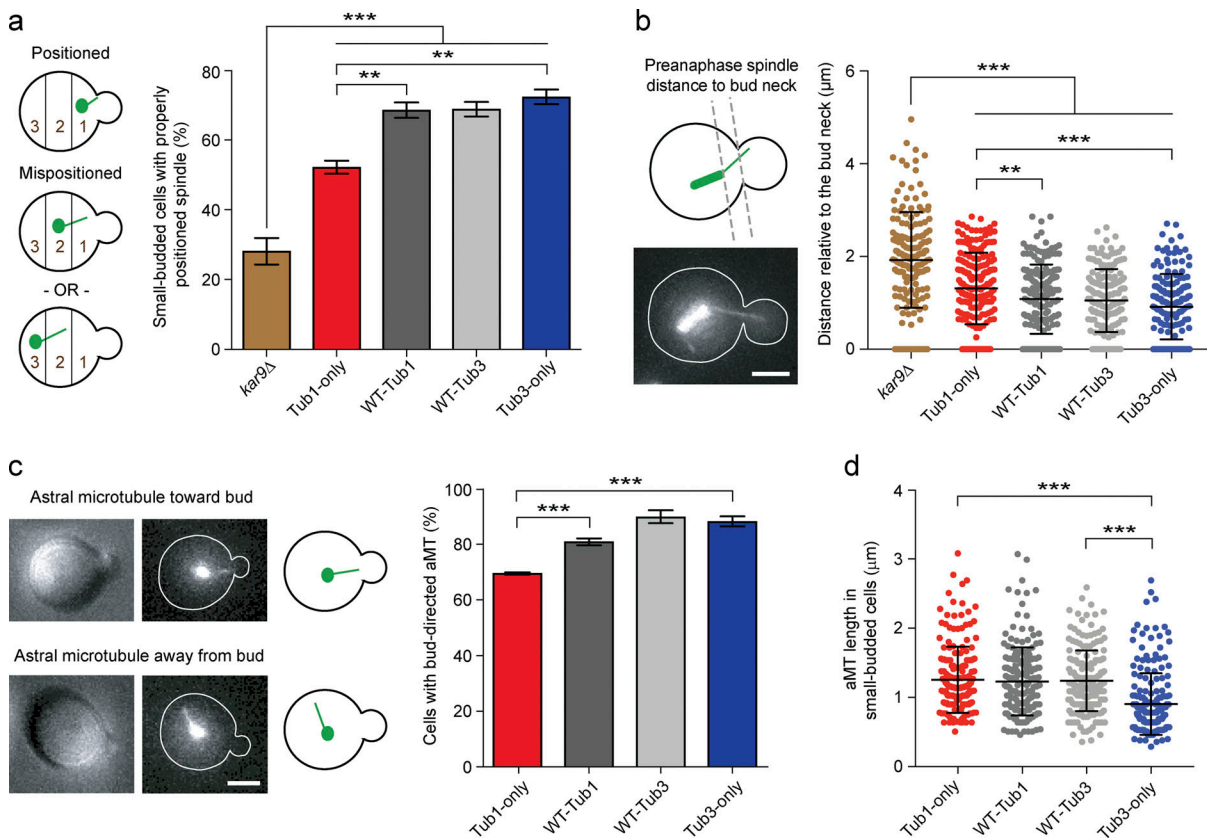


**Figure 7. Tub3 optimizes spindle positioning by the Kar9 pathway. (a)** Small-budded cells of the indicated genotype with properly positioned early mitotic spindles (category 1 on the left). **(b)** Preanaphase spindle positioning relative to the bud neck. Micrograph shows representative GFP-tubulin image with cell outline in white. **(c)** Small-budded cells with early mitotic spindle that display an astral microtubule oriented toward, or away from, the bud. Micrographs show cell (left) and GFP-tubulin image with cell outline in white (right) that are representative of categories shown in cartoons. **(d)** Astral microtubule length in small-budded cells. In panels a and c, bars show mean  $\pm$  SEM from three trials; in panel a, for *kar9Δ*,  $n = 67, 64,$  and  $83$ ; for Tub1 only,  $n = 84, 82,$  and  $94$ ; for WT-Tub1,  $n = 57, 66,$  and  $134$ ; for WT-Tub3,  $n = 52, 79,$  and  $100$ ; for Tub3 only,  $n = 102, 116,$  and  $116$ . In panel c, for Tub1 only,  $n = 65, 65,$  and  $70$ ; for WT-Tub1,  $n = 60, 60,$  and  $58$ ; for WT-Tub3,  $n = 62, 55,$  and  $59$ ; for Tub3 only,  $n = 66, 64,$  and  $55$ . For panels b and d, lines and error bars show mean  $\pm$  SD from three trials. In panel b, scatterplot shows individual cells observed in three trials with a total of 169, 205, 187, 180, and 165 for *kar9Δ*, Tub1 only, WT-Tub1, WT-Tub3, and Tub3 only, respectively. In panel d, scatterplot shows microtubules observed in three trials with a total of 193, 186, 193, and 207 for Tub1 only, WT-Tub1, WT-Tub3, and Tub3 only, respectively. \*\*,  $P \leq 0.01$ ; and \*\*\*,  $P \leq 0.001$  by unpaired, two-tailed Student's  $t$  test. Scale bars = 2  $\mu\text{m}$ . aMT, astral microtubule.

positioning defects in Tub1-only cells. To test this, we introduced an ectopic copy of Bim1 under its native promoter on a centromeric plasmid. Although this extra copy raised the level of Bim1 normally seen at plus ends in control cells, it eliminated the significant difference in localization observed between Tub1-only and control cells (Fig. 8 e). The ectopic Bim1 is functional and rescues the failure of Kar9-mediated microtubule transport and spindle positioning in *bim1Δ* cells (Fig. 8, f and g). Notably, the defective microtubule transport in Tub1-only cells is fully restored by the ectopic Bim1 (Fig. 8 f). Consistent with this, the efficiency of Kar9 pathway function, as measured by spindle positioning, is restored to WT levels (Fig. 8 g).

These results show that Tub3 is required for sufficient localization of Kar9 pathway components to microtubule plus ends and proper functioning of the Kar9 mechanism. Moreover, restoring localization of Bim1, which links Kar9 to plus ends, fully rescues spindle positioning in the absence of Tub3. Together, the data support the conclusion that relative to Tub1, Tub3 is optimized to achieve early spindle positioning and

functions by specific recruitment of Kar9-associated proteins to the microtubule tip.

## Discussion

Most eukaryotes harbor multiple tubulin isotypes that can co-polymerize into microtubules, yet why they possess them has remained largely obscure. Our results provide novel mechanistic insights into how cells use isotypes to optimize microtubule-dependent functions. Due to complications from subunit stoichiometry, posttranslational modifications, and multiple  $\alpha$ - and  $\beta$ -variants, this problem has remained highly intractable in most model systems. We exploited budding yeast to create otherwise isogenic cells expressing single isotypes at levels similar to total tubulin in normal cells (Fig. 2, a–e). This controlled comparison isolated the function of each isotype to provide compelling evidence that they contribute specialized activities to a variety of cellular processes.

Our data uncover a novel role for tubulin isotypes in spindle positioning and provide mechanistic insights into how they

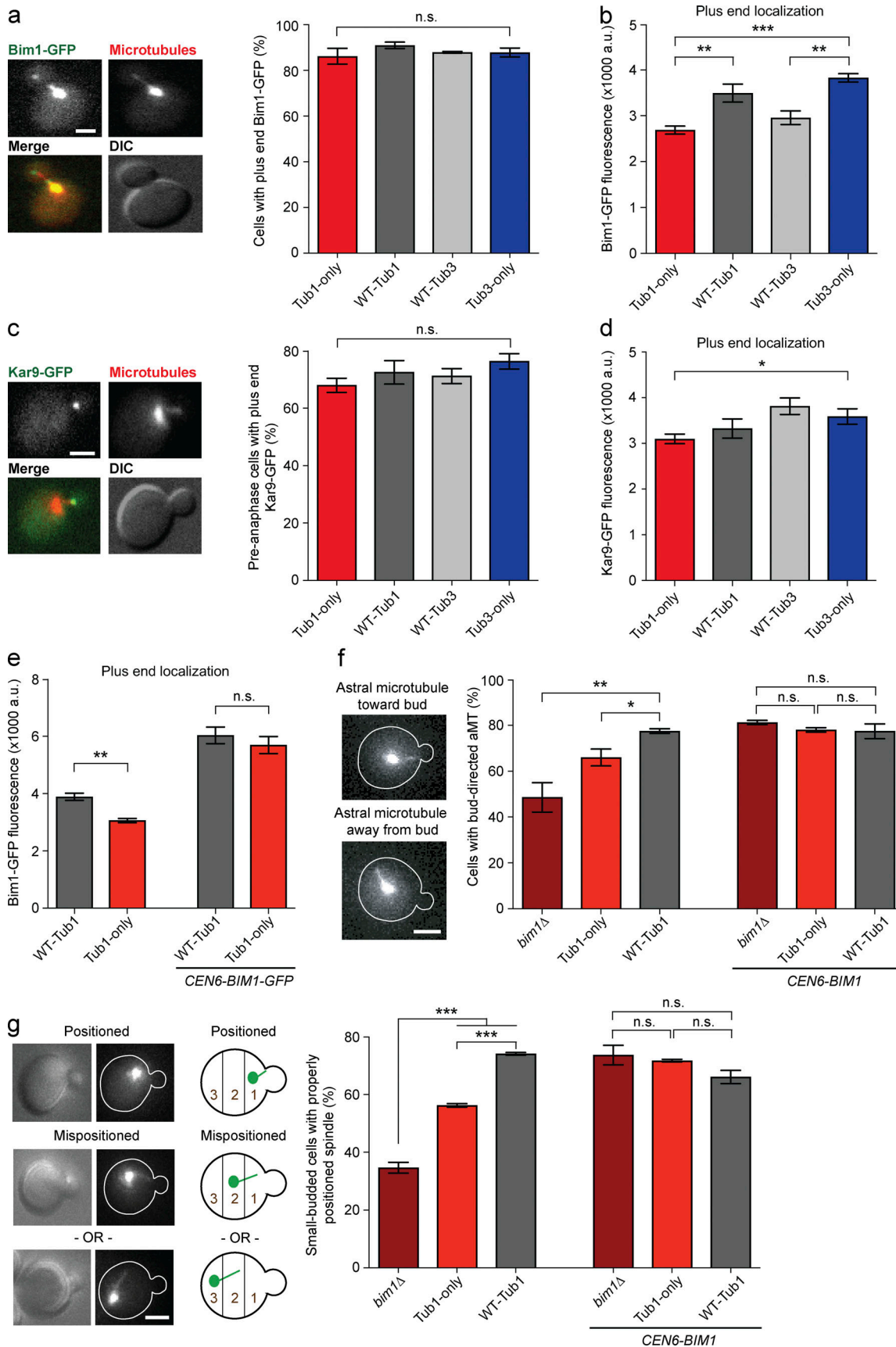


Figure 8. **Tub3 preferentially directs Kar9 pathway proteins to astral microtubule plus ends.** (a) Bim1 localization to microtubule plus ends. Left: Representative wide-field and DIC images of a preanaphase cell showing Bim1-GFP localization to the spindle and astral microtubule plus end. Right:

Percentage of cells with visible Bim1-GFP foci at astral microtubule plus ends. **(b)** Bim1-GFP signal at microtubule plus ends. **(c)** Kar9 localization to microtubule plus ends. Left: Images of a preanaphase cell showing Kar9-GFP localization to astral microtubule plus end. Right: Percentage of cells with visible Kar9-GFP foci at microtubule plus ends. **(d)** Kar9-GFP signal at microtubule plus ends. **(e)** Exogenous *BIMI-GFP* on a centromeric plasmid rescues Bim1 localization to astral microtubules in Tub1-only cells. **(f)** Exogenous *BIMI* restores Kar9-dependent astral microtubule transport to the bud in Tub1-only cells. Number of small-budded cells with early mitotic spindle that display an astral microtubule oriented toward the bud. Micrographs show representative GFP-Tub1 images from each category with cell outline in white. **(g)** Exogenous *BIMI* rescues deficient Kar9-dependent spindle positioning in Tub1-only cells. Micrographs show representative cell (left) and GFP-Tub1 images with cell outline in white (right) from categories shown in cartoons. Bars represent mean  $\pm$  SEM from two trials (a) or three trials (b–g); in panel a, for Tub1 only,  $n = 73$  and  $61$ ; for WT-Tub1,  $n = 82$  and  $56$ ; for WT-Tub3,  $n = 88$  and  $60$ ; for Tub3 only,  $n = 82$  and  $69$ . In panel b, for Tub1 only,  $n = 50, 50,$  and  $65$ ; for WT-Tub1,  $n = 50, 65,$  and  $57$ ; for WT-Tub3,  $n = 50, 56,$  and  $50$ ; for Tub3 only,  $n = 50, 59,$  and  $50$ . In panel c, for Tub1 only,  $n = 61, 51,$  and  $103$ ; for WT-Tub1,  $n = 101, 57,$  and  $79$ ; for WT-Tub3,  $n = 75, 61,$  and  $79$ ; for Tub3 only,  $n = 65, 62,$  and  $95$ . In panel d, for Tub1 only,  $n = 50, 52,$  and  $59$ ; for WT-Tub1,  $n = 61, 60,$  and  $60$ ; for WT-Tub3,  $n = 55, 57,$  and  $60$ ; for Tub3 only,  $n = 59, 59,$  and  $59$ . In panel e, without Bim1 rescue plasmid (left), for Tub1 only,  $n = 48, 44,$  and  $51$ ; for WT-Tub1,  $n = 39, 39,$  and  $48$ ; with Bim1 rescue plasmid (right), for Tub1 only,  $n = 40, 40,$  and  $32$ ; for WT-Tub1,  $n = 38, 40,$  and  $34$ . In panel f, without Bim1 rescue plasmid (left), for *bim1Δ*,  $n = 49, 70,$  and  $59$ ; for Tub1 only,  $n = 46, 55,$  and  $47$ ; for WT-Tub1,  $n = 37, 48,$  and  $49$ ; with Bim1 rescue plasmid (right), for *bim1Δ*,  $n = 49, 46,$  and  $49$ ; for Tub1 only,  $n = 38, 43,$  and  $46$ ; for WT-Tub1,  $n = 38, 50,$  and  $48$ . In panel g, without Bim1 rescue plasmid (left), for *bim1Δ*,  $n = 54, 60,$  and  $65$ ; for Tub1 only,  $n = 61, 47,$  and  $81$ ; for WT-Tub1,  $n = 53, 48,$  and  $57$ ; with Bim1 rescue plasmid (right), for *bim1Δ*,  $n = 63, 69,$  and  $65$ ; for Tub1 only,  $n = 61, 48,$  and  $54$ ; for WT-Tub1,  $n = 47, 62,$  and  $61$ . For panels a and c, merge shows microtubules in red and GFP-tagged proteins in green. n.s., not significant; \*,  $P \leq 0.05$ ; \*\*,  $P \leq 0.01$ ; \*\*\*,  $P \leq 0.001$  by unpaired, two-tailed Student's *t* test. Scale bars =  $2 \mu\text{m}$ ; aMT, astral microtubule.

optimize microtubule-dependent functions. Genome-wide screening with Tub1- and Tub3-only cells revealed diverse categories of synthetic interactions, demonstrating that both isotypes are needed for healthy microtubule function, and lacking either uniquely perturbs cellular processes (Fig. 4, a–c). Notably, the isotypes display distinct genetic relationships with the major mechanisms of mitotic spindle positioning (Fig. 4, d–g). We show that relative to control cells with both isotypes, the Dynein-dependent mechanism is enhanced by microtubules made exclusively of Tub1 and diminished by those made of Tub3 (Fig. 5). Conversely, the Kar9-dependent mechanism functions better with only Tub3 and is compromised by Tub1 (Fig. 7). Mechanistically, we show that the isotypes play opposing roles in localizing key components of the Dynein and Kar9 pathways (Figs. 6 and 8). This localization is correlated with the function of each pathway.

Although increased microtubule stability is correlated with Dynein-dependent sliding (Estrem et al., 2017), our data show that changes in microtubule dynamics cannot explain the isotype-specific enhancement of spindle positioning. While Tub1-only cells have somewhat longer microtubules, those in Tub3-only have lower catastrophe frequency and slower depolymerization, which would also be predicted to positively impact Dynein function. The frequency of Dynein activity is also elevated on Tub1 versus Tub3 microtubules and, at similar lengths, Tub1 microtubules support greater Dynein-mediated translocations. This is true whether microtubules are chemically stabilized or not (Fig. 5). Thus, we conclude that localization of components is likely responsible for the optimal Dynein pathway function mediated by Tub1. It is also possible that during translocation events, Dyn1 or other Dynein pathway components interact more effectively with Tub1 than Tub3 and, vice versa, with Kar9 and Tub3. During Kar9-dependent positioning, microtubule length is also not correlated with the enhanced Kar9 pathway function in Tub3-only cells. Moreover, restoring Bim1 localization, which links Kar9 to plus ends (Lee et al., 2000), rescues Kar9 pathway function in cells lacking Tub3 (Fig. 8, e–g). We conclude Tub1 and Tub3 play specialized roles in the localization of proteins that are needed for proper function of the Dynein and Kar9 pathways, respectively. Overall, the results

demonstrate the mechanism by which tubulin isotypes optimize spindle positioning during yeast mitosis.

Our findings dispel the paradigm that the yeast tubulin isotypes are functionally equivalent. Pioneering studies estimated higher *TUB1* mRNA level relative to *TUB3* (Schatz et al., 1986a) and showed that *TUB3* deletion is tolerated, while loss of *TUB1* is lethal but rescued by increased *TUB3* expression (Schatz et al., 1986b). Thus, the viability differences were proposed to result from relative expression levels. This model is consistent with immunoblotting of cell lysates showing  $\sim 70\%$  Tub1 versus  $\sim 30\%$  Tub3 (Aiken et al., 2019). In contrast, using RT-qPCR, we find similar *TUB1* and *TUB3* mRNA levels in WT cultures (Fig. 3). We also show Tub1 supports viability when expressed solely under the regulation of either locus, whereas Tub3 expressed from either locus does not (Fig. 1, d–f). Moreover, immunoblotting with a monoclonal antibody raised against *S. cerevisiae*  $\alpha$ -tubulin, together with *TUB1* mRNA levels in *tub3Δ* cells, suggests each isotype contributes  $\sim 50\%$  to overall tubulin levels (Figs. 2 e and 3 b). Yeast can selectively down-regulate excess tubulin mRNA at the protein level (Katz et al., 1990). We see this in Tub1-only cells, where excess *TUB1* mRNA is down-regulated at the protein level (Figs. 2 e and 3 b). Previous studies show that in some organisms, the loss of specific tubulin genes can be compensated for by increased protein levels of the remaining isotypes (Latremoliere et al., 2018; Bittermann et al., 2019). In *S. cerevisiae*, the ability of *TUB1* or *TUB3* to compensate total tubulin levels following loss of the other is not readily apparent, as  $\alpha$ -tubulin levels are reduced  $\sim 50\%$  in *tub3Δ* cells, and *tub1Δ* cells are inviable yet can be rescued by boosting Tub3 levels. This is consistent with previous work showing  $\alpha$ -tubulin levels in *tub3Δ* cells are lower than in WT (Gartz Hanson et al., 2016). If yeast could compensate, then *tub3Δ* cells should display near-WT levels of  $\alpha$ -tubulin and *tub1Δ* cells should be viable. It remains unclear why our in vivo results differ from the higher Tub1/Tub3 ratios seen following tubulin purification (Barnes et al., 1992; Bode et al., 2003). It is possible that Tub1 may be more efficiently extracted from cells under the lysis conditions used for purification or that Tub1 better survives the purification conditions/process. Our study and previous in vivo work cited within address steady-state expression and protein levels in

cultures and thus cannot exclude the possibility of regulated expression of either isotype during specific stages of the mitotic or meiotic life cycles. As a result, the relative levels of Tub1 and Tub3 may also be altered in the later-stage log cultures likely reached during harvest of large volumes (Bode et al., 2003) or industrial scale preparations (Barnes et al., 1992) used for previous purifications.

Overall, our data support the conclusion that in log-phase cultures, the *TUB1* and *TUB3* loci contribute similar amounts to the total cellular tubulin. They also suggest that the isotype properties differ sufficiently such that at ~50% normal levels, Tub1 supports one or more essential processes that Tub3 cannot. In support of this, Tub3-only cells are hypersensitive to carbendazim (Fig. 2 f) despite possessing normal tubulin levels and showing increased microtubule stability in vitro (Bode et al., 2003) and in vivo (Table 1). This sensitivity does not likely result from increased drug binding to Tub3- versus Tub1-containing heterodimers, because the carbendazim binding site is on the  $\beta$ -subunit (Li et al., 1996). Instead, it suggests Tub1 and Tub3 differentially influence the functions of regulatory proteins or MAPs in critical cellular processes that render Tub3-only cells hypersensitive and Tub1-only cells resistant to the effects of carbendazim. Collectively, our results demonstrate functional differences between Tub1 and Tub3.

In vitro reconstitution (Panda et al., 1994; Bode et al., 2003; Pamula et al., 2016; Vemu et al., 2017; Orbach and Howard, 2019) and in vivo analysis (Honda et al., 2017) show specific isotypes can affect microtubule dynamics. Perhaps the strongest indication that Tub1 and Tub3 are functionally distinct is the significant differences in dynamics observed in vitro (Bode et al., 2003). Our results allow the first comparison of the same single isotype both in vitro and in cells. In vitro, Tub3 microtubules depolymerize at only 23% the rate of Tub1 polymers (Bode et al., 2003). In cells, Tub3-only microtubules depolymerize at 74% the rate of Tub1 only (Table 1). Although the slower depolymerization in vitro is generally maintained in cells, the tempered extent suggests regulatory proteins in cells can potentially compensate for aspects of isotype-specific dynamics seen in vitro, a finding with implications for understanding diverse cellular process. For example, the  $\beta$ -isotype *TUBB3* increases microtubule dynamics in vitro (Panda et al., 1994; Vemu et al., 2017) and is implicated in radial neuronal migration (Saillour et al., 2014), axon regeneration (Latremoliere et al., 2018), and resistance to microtubule-stabilizing anti-cancer therapies (Parker et al., 2017; Prassanawar and Panda, 2019). Our study highlights the notion that although increased dynamics contributed by *TUBB3* may underlie its role in these processes, the in vivo regulatory contexts must be carefully considered.

Using multiple isotypes allows microtubules to achieve diverse functions. Components of the Kar9 and Dynein pathways evolved to perform functions requiring distinct interactions with tubulin. Using multiple isotypes can relieve constraints imposed by specific mechanisms and allow microtubules to more readily coevolve with various proteins. In this way, Tub1 can optimally fulfill requirements for Dynein pathway components, while Tub3 serves the same for the Kar9 pathway. With multiple isotypes, the cell can build microtubules that perform

both tasks sufficiently rather than achieving one at the expense of the other (Fig. 9). Additionally, our screen results show that the isotypes likely differ in their ability to facilitate multiple processes.

Higher eukaryotes and divergent organisms rely on additional and more specialized microtubule-dependent processes. Diverse regulatory proteins, motors, and MAPs require distinct interactions with tubulin/microtubules for optimal function. Increasing the number of both  $\alpha$ - and  $\beta$ -isotypes would expand the range of processes for which the microtubule can be optimized (Fig. 9 d). Consistent with this model, the *Drosophila* isotypes  $\alpha$ Tub85E and  $\beta$ Tub85D have distinct roles in spermatogenesis and can fulfill those roles when present as a fraction of total tubulin (Hutchens et al., 1997; Hoyle and Raff, 1990). The activities of microtubule-severing proteins (Lu et al., 2004), depolymerases (Ti et al., 2018), and motile kinesins (Silva et al., 2017; Sirajuddin et al., 2014) are influenced by isotype composition. Thus, the role of tubulin isotypes in optimizing divergent mechanisms is likely to be widely conserved. Mutations in specific isotypes are responsible for a number of human neuropathies (Bahi-Buisson et al., 2014), reproductive disorders (Feng et al., 2016), and resistance to anti-cancer therapies (Huzil et al., 2007). Mutations in a given isotype may preferentially affect cellular processes that it optimizes. Therefore, our findings have implications for understanding the function of tubulin isotypes in diverse biological processes as well as human health and disease.

## Materials and methods

### Yeast strains and plasmids

Yeast strains used in this study are derivatives of the S288C background and, together with plasmids, are listed in Table S2. The Tub1-only strain was developed through a fragment-mediated homologous recombination strategy. The endogenous *TUB3* ORF was first replaced with the *URA3* auxotrophic selection gene. Next, the *URA3* marker gene was replaced with a *TUB1* ORF fragment containing homology at the 5' and 3' ends to the endogenous *TUB3* promoter and 3' UTR, respectively. Homologous recombination with this fragment places the *TUB1* ORF seamlessly into the endogenous *TUB3* regulatory elements. Transformants were selected on 5-fluoroorotic acid. The Tub3-only strain was generated using an integrating plasmid and a pop-in/pop-out strategy. To create the plasmid pMG635, a fragment containing, from 5' to 3', 125 bp of *TUB1* 3' UTR beginning immediately after the stop codon, an XhoI site, 140 bp *TUB1* promoter immediately upstream of the start site, and the *TUB3* ORF followed by 200 bp *TUB1* 3' UTR was synthesized in vitro and cloned into the pRS306 vector backbone. Linearization with XhoI results in a pTUB1-TUB3-TUB1 3' UTR-*URA3* plasmid backbone -*TUB1* 3' UTR fragment that integrates at the *TUB1* promoter and 3' UTR sites to replace *TUB1* ORF with that for *TUB3*. Recombination between the duplicate sections of *TUB1* 3' UTR "pops out" the plasmid backbone to seamlessly place the *TUB3* ORF into the endogenous *TUB1* regulatory elements and was selected for on 5-fluoroorotic acid. Strains were verified at each step by PCR analysis and sequencing of recombinant



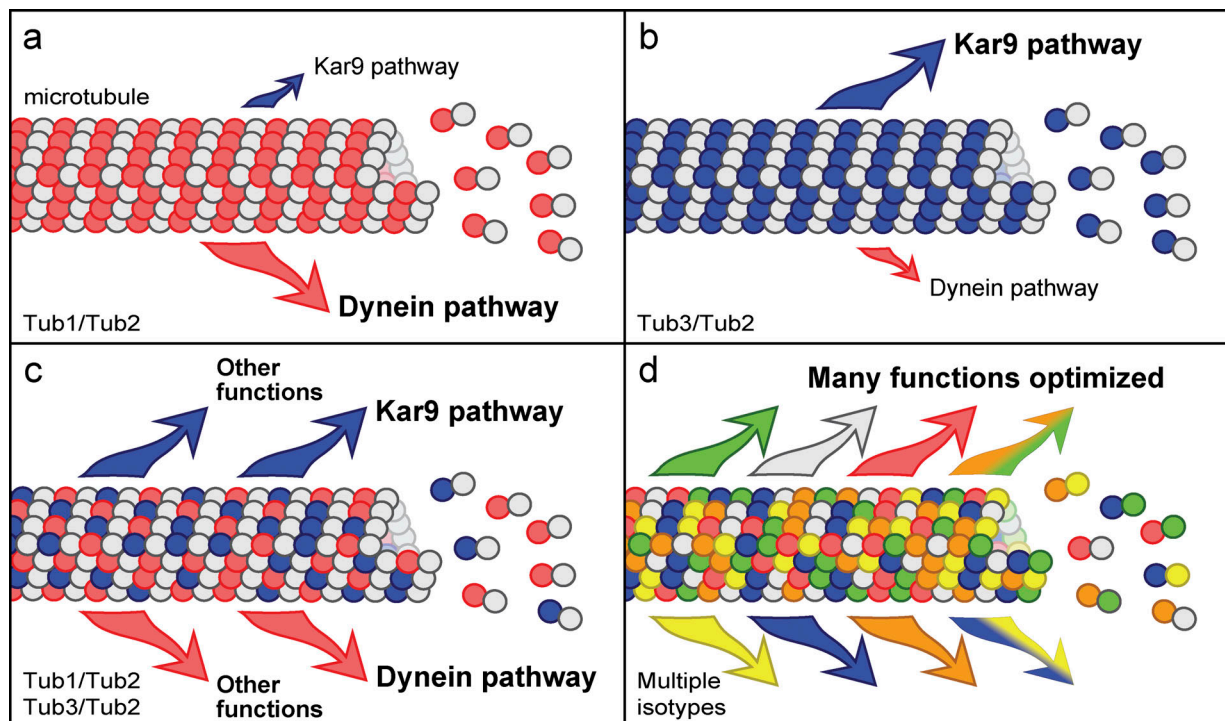


**Figure 9. Model for the role of tubulin isotypes in optimizing diverse microtubule functions.** (a) Yeast microtubules polymerized from only the  $\alpha$ -isotype Tub1 (red) optimize the Dynein-mediated spindle positioning mechanism at the expense of the Kar9 mechanism. (b) Those made from only Tub3 (blue) optimize the Kar9-mediated mechanism at the expense of the Dynein mechanism. (c) In WT cells, microtubules containing both Tub1 and Tub3 support both mechanisms sufficiently. Tub1 and Tub3 are likely to differentially support other microtubule-dependent functions as well. (d) Utilization of multiple  $\alpha$ - and  $\beta$ -isotypes (e.g., in higher eukaryotes) would allow microtubules to be optimized for an increased range of molecular functions.

regions. Final strains were also validated by sequence verification of the entire modified genomic regions. Finally, to follow genetic segregation of the altered loci, the Tub1-only (*tub3 $\Delta$ ::TUB1*) and Tub3-only (*tub1 $\Delta$ ::TUB3*) gene replacements were marked with a tightly linked clonNAT (Nourseothricin) antibiotic resistance cassette. To mark Tub1 only, the clonNAT cassette was integrated 249 bp downstream of the endogenous *TUB3* stop codon. This has no effect on carbendazim sensitivity or growth rate. Integration of the clonNAT cassette similarly downstream of the endogenous *TUB1* locus and nearby *ALO1* resulted in slow growth and smaller colony size. Thus, it was placed 361 bp on the opposite side of the coding sequence for the other neighboring gene *YML083C*, which has no effect on carbendazim sensitivity or growth rate.

Microtubules were visualized using GFP- or mRUBY3-tagged tubulin (Tub1 or Tub3) ectopically expressed from analogous integrated constructs. All constructs were analogous to the *pTUB1-GFP-TUB1* integrating plasmid pAFS125 (Straight et al., 1997). To create the *pTUB1-GFP-TUB3* plasmid, the *TUB1* ORF was excised with flanking BamHI and NotI restriction sites and replaced with the *TUB3* ORF containing identical flanking sequences. To create yeast-optimized mRUBY3 (Bajar et al., 2016) versions of these plasmids, a BamHI site was introduced between *pTUB1* and *GFP* by site-directed mutagenesis (New England Biolabs; Q5). The BamHI sites flanking *GFP* were then used to excise that gene and insert the yeast codon-optimized monomeric RUBY3 ORF synthesized in vitro (Thermo Fisher

Scientific). The *pTUB1-mRUBY3-TUB1* and *pTUB1-mRUBY3-TUB3* region of each plasmid was sequence verified. All four analogous plasmids maintain the same linker sequence between GFP or mRUBY3 and tubulin as found in pAFS125 and are targeted to the *URA3* locus following linearization with StuI. SPBs were visualized using endogenously tagged Cnm67-mRUBY2 (Juanes et al., 2013) introduced into the isotype strains through genetic cross.

For visualization of Kar9 and Dynein pathway components, proteins were tagged with GFP or YFP at their endogenous locus. Previously reported integrating plasmids were used to create Dyn1-GFP (Omer et al., 2018), Bik1-3GFP (Lin et al., 2001), and Kip2-3YFP (Carvalho et al., 2004), while Kar9-GFP (Cuschieri et al., 2006) and Bim1-GFP (Liakopoulos et al., 2003) fusions were created by fragment-mediated tagging as also reported previously. Deletion of genes such as *kar9 $\Delta$ ::HIS3* and *bim1 $\Delta$ ::TRP1* was achieved by fragment-mediated homologous recombination. Tagged and deleted alleles were first introduced and verified in control strains and then crossed with Tub1- and Tub3-only strains to generate mutant and control strains for analyses.

Exogenous Bim1 was expressed from the centromeric plasmid PB2250 (pMG725) containing full-length Bim1 under control of its endogenous promoter. PB2250 (pMG725) is functional in that it fully rescues the spindle positioning defect seen in *bim1 $\Delta$*  cells (Fig. 8, f and g). Plasmid pMG734 was created by introducing GFP in-frame at the C terminus to create *pBIM1-BIM1-GFP*. Details of strain and plasmid construction are available upon request.

### Growth rates and tetrad analysis

To assess growth in liquid medium, fresh overnight cultures were diluted to  $OD_{600} = 0.1$  in YPD (1% yeast extract, 2% peptone, 2% glucose) and incubated with shaking at 24°C, 30°C, and 37°C. To generate a growth curve, the  $OD_{600}$  was monitored every 2 h until cultures reached stationary phase. For growth on solid medium, liquid cultures were grown to saturation for 3 d, and then 10-fold serial dilutions were spotted on YPD plates and incubated for 2 d at 24°C, 30°C, and 37°C. To determine carbendazim sensitivity, 10-fold serial dilutions were spotted onto carbendazim-containing plates as described previously (Luchniak et al., 2013). For genetic crosses and analyses, complete tetrads were confirmed by mating type testing and proper segregation of the genetic markers.

### Genetic screen

To perform SGA analysis with the  $\alpha$ -tubulin isotypes, Tub1-only (*tub3 $\Delta$ ::TUB1*) and Tub3-only (*tub1 $\Delta$ ::TUB3*) mutants were generated in the SGA strain background, and screening was performed as described previously (Baryshnikova et al., 2010). Briefly, the tubulin mutants were crossed to a haploid deletion library (~5,000 genes), and the growth of resulting double mutant progeny was quantitatively determined. Subsequent analysis was performed with only those genes meeting the cutoff for stringent negative genetic interactions, identified as those exhibiting a P value < 0.05 and an SGA interaction score based on colony growth ( $\epsilon$ ) < -0.12 (Costanzo et al., 2010, 2016). Hits meeting these criteria were not validated manually. Venn Diagram Generator (<http://barc.wi.mit.edu/tools/venn/>) was used to display the overlap of stringent negative interactions with loss of TUB1 (*tub1 $\Delta$ ::TUB3*) or TUB3 (*tub3 $\Delta$ ::TUB1*). Enrichment of bioprocess annotation categories within each set of stringent negative interactions was analyzed using TheCellMap (<https://thecellmap.org/>; Usaj et al., 2017) and as previously described (Costanzo et al., 2016). Enrichment is based on the ratio of genes found in our screen from a given category to the total number of genes in the *S. cerevisiae* reference set for that category and displaying  $P < 0.05$  (statistical significance) by Fisher's exact test. The string network of all stringent interactors identified in both screens was constructed using Cytoscape 3.71 (Shannon et al., 2003). SGA interaction scores between microtubule-related genes identified in our SGA screens and components of the Kar9 and Dynein spindle positioning pathways were identified from previously reported SGA interactions in TheCellMap (Usaj et al., 2017), and heatmaps were generated using Prism software (GraphPad). Enrichment was calculated by taking the number of stringent negative interactions as a percentage of total possible interactions between the microtubule-related hits from a given isotype screen and the components of either pathway.

### Live-cell microscopy

Microscopy was performed on an AxioImager M2 microscope (Carl Zeiss) using a 63 $\times$  1.4 NA Plan-APOCHROMAT oil immersion objective with a piezoelectric-driven Z-stage and a CoolSNAP HQ<sup>2</sup> charged-coupled device camera (Photometrics). Briefly, yeast cultures were diluted into synthetic complete medium supplemented with 300  $\mu$ g/ml adenine and grown for

~6 h (over two doublings) at 24°C to reach  $OD_{600} \sim 0.3$ –0.6. Cells were harvested by centrifugation, resuspended in fresh medium, and mounted on 1.2% agarose pads made with the same medium (Luchniak et al., 2013). Unless otherwise noted, cells were imaged at 24°C. GFP, YFP, mRUBY2, and mRUBY3 were visualized with corresponding Semrock filters. Exposure times were optimized based on the fluorescent tag, duration of experiment, and protein of interest. Automated image acquisition was performed in three dimensions using SlideBook software (Intelligent Imaging Innovations) and image analysis was performed using SlideBook and ImageJ (NIH).

### Spindle positioning assays

For spindle positioning assays, cells expressing GFP-Tub1, GFP-Tub3, or Cnm67-mRUBY2 from log-phase cultures were imaged using 12 z-plane stacks at a stepwise distance of 0.75  $\mu$ m. To score spindle position in early mitosis, small-budded cells with unseparated SPBs were partitioned into three equal mother cell segments with regard to bud proximity and categorized according to which segment the center of the unseparated SPBs was positioned. To measure spindle position in preanaphase cells (1–2- $\mu$ m spindle), the distance from the bud neck to the closest SPB was determined using the ruler tool in SlideBook. Mispositioned anaphase spindles were defined as those >3  $\mu$ m that had both SPBs in the mother cell. Those spanning the bud neck with one SPB in the daughter were considered properly positioned. To determine anaphase spindle orientation, only mispositioned spindles were considered, and the offset between the spindle and the mother–bud axes was measured using the angle tool in SlideBook. For an astral microtubule to be considered facing the bud, the orientation of the plus end had to fall within the diameter of the bud neck. All other microtubules were considered to be facing away from the bud.

### Localization of Dynein and Kar9 spindle positioning pathway proteins

To determine the localization of Dyn1-3GFP, Bik1-3GFP, Kip2-3YFP, Kar9-GFP, or Bim1-GFP on mRUBY3-Tub1/Tub3 microtubules, two-color images of cells were captured with 12 z-planes spaced at 0.75  $\mu$ m. Astral microtubule plus end localization was quantified by placing a 12-pixel spot at the plus end in the sum projection of z-series images. Total signal within the spot was adjusted for background by subtracting the intensity of a same sized region directly adjacent to the plus end being quantified. SPB localization was quantified on the bud-proximal SPBs that displayed visible fluorescent foci. Cortical foci were identified by cross referencing with differential interference contrast (DIC) and mRUBY3-Tub1/Tub3 images to confirm cortical position and rule out microtubule localization, respectively. Dyn1-3GFP, Bik1-3GFP, and Kip2-3YFP localization was determined in early anaphase cells (medium/large size bud with spindle  $\geq 3$   $\mu$ m positioned within mother cell or adjacent to the bud neck). Kar9-GFP and Bim1-GFP were localized in pre-anaphase cells (bud <1/4 mother cell diameter with spindle <2  $\mu$ m). Astral microtubules with multiple Bik1-3GFP foci were identified visually in anaphase cells (medium/large size bud with spindle  $\geq 3$   $\mu$ m).

### Imaging and analysis of microtubule dynamics

Microtubule dynamics was analyzed in HU-treated (200 mM, 2.5 h), S-phase-arrested cells using 10-min time-lapse movies of GFP-Tub1 or GFP-Tub3 imaged at 4-s intervals using seven z-planes spaced at 0.75  $\mu\text{m}$ . Microtubule plus ends were enhanced by Bik1-3GFP expressed from the endogenous locus. Astral microtubule length at each time point was determined in 3D using the average of two independent measurements. Microtubule polymerization or depolymerization events were defined as four or more contiguous time points resulting in a  $\geq 0.6\text{-}\mu\text{m}$  length change with  $R^2 \geq 0.8$ . Length changes  $\leq \pm 0.2\text{ }\mu\text{m}$  throughout four or more contiguous time points were defined as pause. Transition from polymerization or pause to depolymerization was defined as catastrophe. Transition from depolymerization to pause or polymerization was defined as rescue. Catastrophe frequency was determined by dividing the total number of catastrophes by the total time microtubules spent in polymerization and pause. Rescue frequency was calculated by dividing the total number of rescues by the total time in depolymerization. Dynamicity was measured by calculating total change in length due to polymerization and depolymerization over time and converting to tubulin molecules (1,690 heterodimers/ $\mu\text{m}$ ) exchanged per second at the plus end. Microtubule dynamics data were compiled from images obtained on two independent days, in which  $\sim 25$  microtubules from  $\sim 15$  cells were analyzed for each genotype from each day. To determine average length, astral microtubules were measured using single-time point 3D images of G1 and anaphase cells.

### Imaging and analysis of Dynein-mediated spindle movement

Dynein activity was quantified in HU-treated (200 mM, 2.5 h), S-phase-arrested cells using 10-min time-lapse movies of GFP-Tub1 or GFP-Tub3, captured at 8-s intervals by seven to nine z-planes spaced 0.75  $\mu\text{m}$  apart. For Dynein activity during epothilone B treatment, drug-sensitized cells (*pdr1 $\Delta$  pdr3 $\Delta$* ) in mid-log phase were arrested in HU for 90 min, followed by addition of 10  $\mu\text{M}$  epothilone B (Selleck Chemical; #S1364) for the remaining 60 min before mounting on a synthetic complete + HU + epothilone B agarose pad. Microtubule plus ends were enhanced by Bik1-3GFP expressed from the endogenous locus. Both GFP and DIC images were taken at every frame. For analysis, 2D maximum projection GFP images were cross-referenced against the center plane DIC image to determine astral microtubule position relative to cell cortex. Microtubule-cortex interactions were scored when the astral microtubule plus end contacted the cortical surface. Dynein activity was defined as spindle movement that occurred as a result of microtubule sliding through lateral interaction with the cortex (Estrem et al., 2017), as well as end-on interaction with the cortex (Omer et al., 2018). The distance and duration of spindle movement toward the point of microtubule-cortex interaction was determined from the time-lapse images beginning at the first instance of directed spindle movement upon microtubule-cortex interaction and ending with cessation of spindle movement. Astral microtubule length at the start of Dynein activity was measured using the image in which directed spindle movement initiated. The Dynein activity analysis was

performed using time-lapse images of 90–100 cells for each genotype obtained from three independent trials.

### Protein extraction and Western blot analysis

Overnight cultures were diluted to  $\text{OD}_{600} = 0.1$  in 10 ml YPD and grown for 6 h before cells were harvested by centrifugation for 5 min at 3,000  $g$ . Cells were resuspended in 1 ml ice-cold 0.1 M NaOH and incubated for 15 min on ice while gently inverting the tubes every few minutes. The samples were centrifuged for 2 min at 3,000  $g$ , and after discarding the supernatant, the pelleted cells were resuspended in 150  $\mu\text{l}$  1X SDS-gel sample loading buffer (50 mM Tris-Cl, pH 6.8, 2% SDS, 10% glycerol, 100 mM DTT, and 0.06% bromophenol blue) and heated to 95°C for 10 min, and soluble protein was loaded on SDS-PAGE after elimination of cellular debris by centrifugation (10 min at 20,000  $g$ ). Lysates were resolved on an 8% Tris-Gly gel by SDS-PAGE and transferred to a polyvinylidene fluoride membrane for blotting. Band intensities were quantified using SlideBook software. Relative tubulin levels were calculated by dividing tubulin band intensity by that of actin and normalizing to the tubulin/actin ratio in control cells. Tubulin and actin band intensities were verified to be linear with respect to sample loading over a plus/minus twofold range relative to that used for quantification. The antibody monoclonal rat anti- $\alpha$ -tubulin YOL1/34 (Thermo Fisher Scientific; #MA1-80189) was used at 1:5,000 dilution, while monoclonal mouse anti-actin (Abcam; #ab8224) was used at 1:2,000. HRP-linked anti-rat (GE Healthcare; #NA935) and anti-mouse (GE Healthcare; #NA931) secondary antibodies were used at 1:10,000 dilution and detected by enhanced chemiluminescence (GE Healthcare; #RPN3243).

### RNA extraction and real-time RT-qPCR

Total RNA was extracted from yeast cultures grown in 10 ml YPD at 30°C to an  $\text{OD}_{600} = 0.5\text{--}0.8$  by the hot acid phenol extraction method, as described previously (Iyer and Struhl, 1996). RNA was treated with RNA-free DNase (Qiagen; #79254) to digest contaminating DNA before RNA cleanup and purified with the RNeasy mini kit (Qiagen; #74104). cDNA synthesis was performed using the Omniscript Reverse Transcription Kit (Qiagen; #205111) with 10 ng RNA per 20- $\mu\text{l}$  reaction. Real-time RT-qPCR was performed with the QuantStudio 3 Real-Time PCR system (Thermo Fisher Scientific) using the TaqMan Gene Expression Assays (Thermo Fisher Scientific; #4351372) pre-designed for *TUB1* (#ScO4175846\_s1), *TUB3* (#ScO4175861\_s1), and *TUB2* (#ScO4120471\_s1), with *ACT1* (actin; #ScO4120488\_s1) as the internal reference gene control. *TUB1* expression in Tub1-only and WT cells was additionally validated using a custom probe (MGB; 5'-TGCCACACCAAACCTCACAAATTGGCC-3'; Thermo Fisher Scientific) and a different set of primers (5'-TGGTTTCAAGATCGGTATTTGC-3' and 5'-CTCAGCAATGGATGTGGTATT-3'). Real-time RT-qPCR for 3'-UTR-specific transcript expression was done with a custom probe with 100% homology to both the *TUB1* and *TUB3* ORFs (QSY; 5'-TGGTATGTCGGTGAA GGTATGGAAGAAGGTGA-3'; Thermo Fisher Scientific) and a forward primer that also has 100% homology to both *TUB1* and *TUB3* sequences (5'-GTATGCCAAACGTGCTTTTCG-3'). The reverse primers for the endogenous *TUB1* and *TUB3* loci 3' UTR-

specific transcripts were 5'-GAAAGGATAAGGAGTTGGG-3' and 5'-TAAGTGGGTATCGGGATCAG-3', respectively. As validation, all assays had efficiency ~95–100%, the *TUB3* assay detected no transcript in Tub1-only cells, neither *TUB1* assay detected transcript in Tub3-only cells, and the 3' UTR-specific transcript assay failed to detect expression from the *TUB3* locus when the tubulin ORF was replaced with *URA3*. Relative quantification of gene expression was performed using the comparative quantification method ( $\Delta\Delta Ct$ ).

### Statistical analyses and reproducibility

Unless otherwise noted, statistical significance (*P* values) was determined using the unpaired, two-tailed Student's *t* test. Data distribution was assumed to be normal, but this was not formally tested. Linear regression analysis ( $R^2$ ) of microtubule polymerization and depolymerization was performed using Excel software (Microsoft). For SGA screen enrichment, *P* values were evaluated with Fisher's exact test. Sample sizes and number of replicates can be found in the corresponding figure legends. All statistical analyses were performed using Excel (Microsoft) or Prism (GraphPad) software. \*,  $P \leq 0.05$ ; \*\*,  $P \leq 0.01$ ; \*\*\*,  $P \leq 0.001$ ; \*\*\*\*,  $P \leq 0.0001$ .

### Contact for reagent and resource sharing

Further information and requests for resources and reagents should be directed to and will be fulfilled by the lead contact, Mohan Gupta (mgupta@iastate.edu).

### Online supplemental material

[Fig. S1](#) demonstrates that Tub1-only and Tub3-only cells grow at rates similar to control cells and that quantification of *TUB1* transcript is comparable using predesigned TaqMan or custom assays. [Fig. S2](#) compares SGA hits identified in our loss of *TUB3* screen with those found in a previously reported *tub3Δ* screen. [Fig. S3](#) provides evidence that Tub1 orients anaphase spindles via the Dynein mechanism more efficiently than Tub3 and that Dynein localization at the bud cortex and SPB, as well as the proportion of cells with plus end foci of Bik1, are unchanged in Tub1-only and Tub3-only cells. [Fig. S4](#) shows that Dynein pathway function is enhanced in Tub1-only versus Tub3-only cells during epothilone treatment that stabilizes astral microtubules. [Fig. S5](#) displays representative lifetime history plots of astral microtubules in HU-arrested, mock-treated, and epothilone-treated Tub1-only, Tub3-only, and control cells. [Fig. S6](#) demonstrates, using RUBY2-tagged SPBs instead of GFP-tagged tubulin, that Tub3 optimizes Kar9-dependent spindle positioning. The six videos present representative time-lapse images of HU-arrested (S-phase) cells. [Video 1](#) depicts Dynein-mediated spindle sliding. [Video 2](#) shows astral microtubule dynamics in an untreated control cell. [Video 3](#) shows astral microtubule dynamics in an untreated Tub1-only cell. [Video 4](#) shows astral microtubule dynamics in an untreated Tub3-only cell. [Video 5](#) shows astral microtubule dynamics in a mock-treated Tub3-only cell. [Video 6](#) shows astral microtubule dynamics in an epothilone B-treated Tub3-only cell. Table S1 contains the full list of positive and negative synthetic genetic interactions for *tub1Δ::TUB3* (loss of *TUB1*) and *tub3Δ::TUB1* (loss of *TUB3*) SGA screens. Table S2 lists all yeast strains and plasmids used in this study.

## Acknowledgments

We thank W.-L. Lee (Dartmouth College, Hanover, NH), J. Moore (University of Colorado Medical School, Denver, CO), and D. Pellman (Dana-Farber Cancer Institute, Boston, MA) for useful reagents and are grateful to S. Anderson for helpful feedback.

C. Boone is a senior fellow in the Canadian Institutes of Health Research Fungal Kingdom: Threats & Opportunities program. This work was supported by the Canadian Institutes of Health Research (grant FDN-143264), the National Institutes of Health (grant R01HG005853 to C. Boone), and National Science Foundation (grant MCB-1846262 to M.L. Gupta).

The authors declare no competing financial interests.

Author contributions: M.L. Gupta conceived of the project; E.T. Nsamba, A. Bera, and M.L. Gupta designed the research and constructed reagents; E.T. Nsamba, A. Bera, M. Costanzo, C. Boone, and M.L. Gupta performed experiments and analyzed data; E.T. Nsamba, A. Bera, and M.L. Gupta prepared figures and wrote the manuscript.

Submitted: 26 October 2020

Revised: 6 September 2021

Accepted: 12 October 2021

## References

- Adames, N.R., and J.A. Cooper. 2000. Microtubule interactions with the cell cortex causing nuclear movements in *Saccharomyces cerevisiae*. *J. Cell Biol.* 149:863–874. <https://doi.org/10.1083/jcb.149.4.863>
- Aiken, J., J.K. Moore, and E.A. Bates. 2019. TUBA1A mutations identified in lissencephaly patients dominantly disrupt neuronal migration and impair dynein activity. *Hum. Mol. Genet.* 28:1227–1243. <https://doi.org/10.1093/hmg/ddy416>
- Bahi-Buisson, N., K. Poirier, F. Fourniol, Y. Saillour, S. Valence, N. Lebrun, M. Hully, C.F. Bianco, N. Boddaert, C. Elie, et al. LIS-Tubulinopathies Consortium. 2014. The wide spectrum of tubulinopathies: what are the key features for the diagnosis? *Brain.* 137:1676–1700. <https://doi.org/10.1093/brain/awu082>
- Bajar, B.T., E.S. Wang, A.J. Lam, B.B. Kim, C.L. Jacobs, E.S. Howe, M.W. Davidson, M.Z. Lin, and J. Chu. 2016. Improving brightness and photostability of green and red fluorescent proteins for live cell imaging and FRET reporting. *Sci. Rep.* 6:20889. <https://doi.org/10.1038/srep20889>
- Baran, R., L. Castelblanco, G. Tang, I. Shapiro, A. Goncharov, and Y. Jin. 2010. Motor neuron synapse and axon defects in a *C. elegans* alpha-tubulin mutant. *PLoS One.* 5:e9655. <https://doi.org/10.1371/journal.pone.0009655>
- Barnes, G., K.A. Louie, and D. Botstein. 1992. Yeast proteins associated with microtubules in vitro and in vivo. *Mol. Biol. Cell.* 3:29–47. <https://doi.org/10.1091/mbc.3.1.29>
- Baryshnikova, A., M. Costanzo, Y. Kim, H. Ding, J. Koh, K. Toufighi, J.-Y. Youn, J. Ou, B.J. San Luis, S. Bandyopadhyay, et al. 2010. Quantitative analysis of fitness and genetic interactions in yeast on a genome scale. *Nat. Methods.* 7:1017–1024. <https://doi.org/10.1038/nmeth.1534>
- Bittermann, E., Z. Abdelhamed, R.P. Liegel, C. Menke, A. Timms, D.R. Beier, and R.W. Stottmann. 2019. Differential requirements of tubulin genes in mammalian forebrain development. *PLoS Genet.* 15:e1008243. <https://doi.org/10.1371/journal.pgen.1008243>
- Bodakuntla, S., A.S. Jijumon, C. Villablanca, C. Gonzalez-Billault, and C. Janke. 2019. Microtubule-Associated Proteins: Structuring the Cytoskeleton. *Trends Cell Biol.* 29:804–819. <https://doi.org/10.1016/j.tcb.2019.07.004>
- Bode, C.J., M.L. Gupta, K.A. Suprenant, and R.H. Himes. 2003. The two  $\alpha$ -tubulin isotypes in budding yeast have opposing effects on microtubule dynamics in vitro. *EMBO Rep.* 4:94–99. <https://doi.org/10.1038/sj.embor.embor716>
- Breitling, F., and M. Little. 1986. Carboxy-terminal regions on the surface of tubulin and microtubules. Epitope locations of YOL1/34, DM1A and DM1B. *J. Mol. Biol.* 189:367–370. [https://doi.org/10.1016/0022-2836\(86\)90517-6](https://doi.org/10.1016/0022-2836(86)90517-6)

- Burke, D., P. Gasdaska, and L. Hartwell. 1989. Dominant effects of tubulin overexpression in *Saccharomyces cerevisiae*. *Mol. Cell. Biol.* 9:1049–1059. <https://doi.org/10.1128/MCB.9.3.1049>
- Carvalho, P., M.L. Gupta Jr., M.A. Hoyt, and D. Pellman. 2004. Cell cycle control of kinesin-mediated transport of Bik1 (CLIP-170) regulates microtubule stability and dynein activation. *Dev. Cell.* 6:815–829. <https://doi.org/10.1016/j.devcel.2004.05.001>
- Costanzo, M., A. Baryshnikova, J. Bellay, Y. Kim, E.D. Spear, C.S. Sevier, H. Ding, J.L.Y. Koh, K. Toufighi, S. Mostafavi, et al. 2010. The genetic landscape of a cell. *Science.* 327:425–431. <https://doi.org/10.1126/science.1180823>
- Costanzo, M., B. VanderSluis, E.N. Koch, A. Baryshnikova, C. Pons, G. Tan, W. Wang, M. Usaj, J. Hanchard, S.D. Lee, et al. 2016. A global genetic interaction network maps a wiring diagram of cellular function. *Science.* 353:aaf1420. <https://doi.org/10.1126/science.aaf1420>
- Cuschieri, L., R. Miller, and J. Vogel. 2006.  $\gamma$ -tubulin is required for proper recruitment and assembly of Kar9-Bim1 complexes in budding yeast. *Mol. Biol. Cell.* 17:4420–4434. <https://doi.org/10.1091/mbc.e06-03-0245>
- Detrich, H.W. III, V. Prasad, and R.F. Ludueña. 1987. Cold-stable microtubules from Antarctic fishes contain unique alpha tubulins. *J. Biol. Chem.* 262: 8360–8366. [https://doi.org/10.1016/S0021-9258\(18\)47572-2](https://doi.org/10.1016/S0021-9258(18)47572-2)
- Estrem, C., C.P. Fees, and J.K. Moore. 2017. Dynein is regulated by the stability of its microtubule track. *J. Cell Biol.* 216:2047–2058. <https://doi.org/10.1083/jcb.201611105>
- Feng, R., Q. Sang, Y. Kuang, X. Sun, Z. Yan, S. Zhang, J. Shi, G. Tian, A. Luchniak, Y. Fukuda, et al. 2016. Mutations in TUBB8 and Human Oocyte Meiotic Arrest. *N. Engl. J. Med.* 374:223–232. <https://doi.org/10.1056/NEJMoa1510791>
- Fulton, C., and P.A. Simpson. 1976. Selective synthesis and utilization of flagellar tubulin. The multi-tubulin hypothesis. *Cell Motil. Cytoskeleton.* 3:987–1005.
- Gartz Hanson, M., J. Aiken, D.V. Sietsema, D. Sept, E.A. Bates, L. Niswander, and J.K. Moore. 2016. Novel  $\alpha$ -tubulin mutation disrupts neural development and tubulin proteostasis. *Dev. Biol.* 409:406–419. <https://doi.org/10.1016/j.ydbio.2015.11.022>
- Guiltinan, M.J., D.P. Ma, R.F. Barker, M.M. Bustos, R.J. Cyr, R. Yadegari, and D.E. Fosket. 1987. The isolation, characterization and sequence of two divergent  $\beta$ -tubulin genes from soybean (*Glycine max* L.). *Plant Mol. Biol.* 10:171–184. <https://doi.org/10.1007/BF00016154>
- Honda, Y., K. Tsuchiya, E. Sumiyoshi, N. Haruta, and A. Sugimoto. 2017. Tubulin isotype substitution revealed that isotype combination modulates microtubule dynamics in *C. elegans* embryos. *J. Cell Sci.* 130: 1652–1661. <https://doi.org/10.1242/jcs.200923>
- Hoyle, H.D., and E.C. Raff. 1990. Two *Drosophila* beta tubulin isoforms are not functionally equivalent. *J. Cell Biol.* 111:1009–1026. <https://doi.org/10.1083/jcb.111.3.1009>
- Hurd, D.D., R.M. Miller, L. Núñez, and D.S. Portman. 2010. Specific alpha and beta-tubulin isotypes optimize the functions of sensory cilia in *Caenorhabditis elegans*. *Genetics.* 185:883–896. <https://doi.org/10.1534/genetics.110.116996>
- Hutchens, J.A., H.D. Hoyle, F.R. Turner, and E.C. Raff. 1997. Structurally similar *Drosophila* alpha-tubulins are functionally distinct in vivo. *Mol. Biol. Cell.* 8:481–500. <https://doi.org/10.1091/mbc.8.3.481>
- Huzil, J.T., K. Chen, L. Kurgan, and J.A. Tuszynski. 2007. The roles of  $\beta$ -tubulin mutations and isotype expression in acquired drug resistance. *Cancer Inform.* 3:159–181. <https://doi.org/10.1177/117693510700300028>
- Iyer, V., and K. Struhl. 1996. Absolute mRNA levels and transcriptional initiation rates in *Saccharomyces cerevisiae*. *Proc. Natl. Acad. Sci. USA.* 93: 5208–5212. <https://doi.org/10.1073/pnas.93.11.5208>
- Janke, C., and M.M. Magiera. 2020. The tubulin code and its role in controlling microtubule properties and functions. *Nat. Rev. Mol. Cell Biol.* 21: 307–326. <https://doi.org/10.1038/s41580-020-0214-3>
- Juanes, M.A., H. Twyman, E. Tunnacliffe, Z. Guo, R. ten Hoopen, and M. Segal. 2013. Spindle pole body history intrinsically links pole identity with asymmetric fate in budding yeast. *Curr. Biol.* 23:1310–1319. <https://doi.org/10.1016/j.cub.2013.05.057>
- Katz, W., B. Weinstein, and F. Solomon. 1990. Regulation of tubulin levels and microtubule assembly in *Saccharomyces cerevisiae*: consequences of altered tubulin gene copy number. *Mol. Cell. Biol.* 10:5286–5294. <https://doi.org/10.1128/MCB.10.10.5286>
- Krauh, E., M. Little, T. Kempf, R. Hofer-Warbinek, W. Ade, and H. Ponstingl. 1981. Complete amino acid sequence of beta-tubulin from porcine brain. *Proc. Natl. Acad. Sci. USA.* 78:4156–4160. <https://doi.org/10.1073/pnas.78.7.4156>
- Latremoliere, A., L. Cheng, M. DeLisle, C. Wu, S. Chew, E.B. Hutchinson, A. Sheridan, C. Alexandre, F. Latremoliere, S.-H. Sheu, et al. 2018. Neuronal-Specific TUBB3 Is Not Required for Normal Neuronal Function but Is Essential for Timely Axon Regeneration. *Cell Rep.* 24: 1865–1879.e9. <https://doi.org/10.1016/j.celrep.2018.07.029>
- Lee, L., J.S. Tirnauer, J. Li, S.C. Schuyler, J.Y. Liu, and D. Pellman. 2000. Positioning of the mitotic spindle by a cortical-microtubule capture mechanism. *Science.* 287:2260–2262. <https://doi.org/10.1126/science.287.5461.2260>
- Lee, W.-L., J.R. Oberle, and J.A. Cooper. 2003. The role of the lissencephaly protein Pacl during nuclear migration in budding yeast. *J. Cell Biol.* 160: 355–364. <https://doi.org/10.1083/jcb.200209022>
- Li, J., S.K. Katiyar, and T.D. Edlind. 1996. Site-directed mutagenesis of *Saccharomyces cerevisiae*  $\beta$ -tubulin: interaction between residue 167 and benzimidazole compounds. *FEBS Lett.* 385:7–10. [https://doi.org/10.1016/0014-5793\(96\)00334-1](https://doi.org/10.1016/0014-5793(96)00334-1)
- Liakopoulos, D., J. Kusch, S. Grava, J. Vogel, and Y. Barral. 2003. Asymmetric loading of Kar9 onto spindle poles and microtubules ensures proper spindle alignment. *Cell.* 112:561–574. [https://doi.org/10.1016/S0092-8674\(03\)00119-3](https://doi.org/10.1016/S0092-8674(03)00119-3)
- Lin, H., P. de Carvalho, D. Kho, C.-Y. Tai, P. Pierre, G.R. Fink, and D. Pellman. 2001. Polyploids require Bik1 for kinetochore-microtubule attachment. *J. Cell Biol.* 155:1173–1184. <https://doi.org/10.1083/jcb.200108119>
- Little, M., and T. Seehaus. 1988. Comparative analysis of tubulin sequences. *Comp. Biochem. Physiol. B.* 90:655–670. [https://doi.org/10.1016/0305-0491\(88\)90320-3](https://doi.org/10.1016/0305-0491(88)90320-3)
- Lockhead, D., E.M. Schwarz, R. O'Hagan, S. Bellotti, M. Krieg, M.M. Barr, A.R. Dunn, P.W. Sternberg, and M.B. Goodman. 2016. The tubulin repertoire of *C. elegans* sensory neurons and its context-dependent role in process outgrowth. *Mol. Biol. Cell.* 27:3717–3728. <https://doi.org/10.1091/mbc.e16-06-0473>
- Lu, C., M. Srayko, and P.E. Mains. 2004. The *Caenorhabditis elegans* microtubule-severing complex MEI-1/MEI-2 katanin interacts differently with two superficially redundant  $\beta$ -tubulin isotypes. *Mol. Biol. Cell.* 15:142–150. <https://doi.org/10.1091/mbc.e03-06-0418>
- Luchniak, A., Y. Fukuda, and M.L. Gupta Jr. 2013. Structure-function analysis of yeast tubulin. *Methods Cell Biol.* 115:355–374. <https://doi.org/10.1016/B978-0-12-407757-7.00022-0>
- McNally, F.J. 2013. Mechanisms of spindle positioning. *J. Cell Biol.* 200: 131–140. <https://doi.org/10.1083/jcb.201210007>
- Miller, R.K., K.K. Heller, L. Frisèn, D.L. Wallack, D. Loayza, A.E. Gammie, and M.D. Rose. 1998. The kinesin-related proteins, Kip2p and Kip3p, function differently in nuclear migration in yeast. *Mol. Biol. Cell.* 9: 2051–2068. <https://doi.org/10.1091/mbc.9.8.2051>
- Minoura, I., Y. Hachikubo, Y. Yamakita, H. Takazaki, R. Ayukawa, S. Uchi-mura, and E. Muto. 2013. Overexpression, purification, and functional analysis of recombinant human tubulin dimer. *FEBS Lett.* 587:3450–3455. <https://doi.org/10.1016/j.febslet.2013.08.032>
- Neff, N.F., J.H. Thomas, P. Grisafi, and D. Botstein. 1983. Isolation of the beta-tubulin gene from yeast and demonstration of its essential function in vivo. *Cell.* 33:211–219. [https://doi.org/10.1016/0092-8674\(83\)90350-1](https://doi.org/10.1016/0092-8674(83)90350-1)
- Nogales, E. 2000. Structural insights into microtubule function. *Annu. Rev. Biochem.* 69:277–302. <https://doi.org/10.1146/annurev.biochem.69.1.277>
- Omer, S., S.R. Greenberg, and W.-L. Lee. 2018. Cortical dynein pulling mechanism is regulated by differentially targeted attachment molecule Num1. *eLife.* 7:e36745. <https://doi.org/10.7554/eLife.36745>
- Orbach, R., and J. Howard. 2019. The dynamic and structural properties of axonemal tubulins support the high length stability of cilia. *Nat. Commun.* 10:1838. <https://doi.org/10.1038/s41467-019-09779-6>
- Pamula, M.C., S.-C. Ti, and T.M. Kapoor. 2016. The structured core of human  $\beta$  tubulin confers isotype-specific polymerization properties. *J. Cell Biol.* 213:425–433. <https://doi.org/10.1083/jcb.201603050>
- Panda, D., H.P. Miller, A. Banerjee, R.F. Ludueña, and L. Wilson. 1994. Microtubule dynamics in vitro are regulated by the tubulin isotype composition. *Proc. Natl. Acad. Sci. USA.* 91:11358–11362. <https://doi.org/10.1073/pnas.91.24.11358>
- Parker, A.L., W.S. Teo, J.A. McCarroll, and M. Kavallaris. 2017. An Emerging Role for Tubulin Isoforms in Modulating Cancer Biology and Chemotherapy Resistance. *Int. J. Mol. Sci.* 18:1434. <https://doi.org/10.3390/ijms18071434>
- Prassanawar, S.S., and D. Panda. 2019. Tubulin heterogeneity regulates functions and dynamics of microtubules and plays a role in the development of drug resistance in cancer. *Biochem. J.* 476:1359–1376. <https://doi.org/10.1042/BCJ20190123>

- Pratt, L.F., and D.W. Cleveland. 1988. A survey of the alpha-tubulin gene family in chicken: unexpected sequence heterogeneity in the polypeptides encoded by five expressed genes. *EMBO J.* 7:931–940. <https://doi.org/10.1002/j.1460-2075.1988.tb02898.x>
- Richards, K.L., K.R. Anders, E. Nogales, K. Schwartz, K.H. Downing, and D. Botstein. 2000. Structure-function relationships in yeast tubulins. *Mol. Biol. Cell.* 11:1887–1903. <https://doi.org/10.1091/mbc.11.5.1887>
- Saillour, Y., L. Broix, E. Bruel-Jungerman, N. Lebrun, G. Muraca, J. Rucci, K. Poirier, R. Belvindrah, F. Francis, and J. Chelly. 2014. Beta tubulin isoforms are not interchangeable for rescuing impaired radial migration due to Tubb3 knockdown. *Hum. Mol. Genet.* 23:1516–1526. <https://doi.org/10.1093/hmg/ddt538>
- Schatz, P.J., L. Pillus, P. Grisafi, F. Solomon, and D. Botstein. 1986a. Two functional alpha-tubulin genes of the yeast *Saccharomyces cerevisiae* encode divergent proteins. *Mol. Cell. Biol.* 6:3711–3721. <https://doi.org/10.1128/MCB.6.11.3711>
- Schatz, P.J., F. Solomon, and D. Botstein. 1986b. Genetically essential and nonessential alpha-tubulin genes specify functionally interchangeable proteins. *Mol. Cell. Biol.* 6:3722–3733. <https://doi.org/10.1128/MCB.6.11.3722>
- Shannon, P., A. Markiel, O. Ozier, N.S. Baliga, J.T. Wang, D. Ramage, N. Amin, B. Schwikowski, and T. Ideker. 2003. Cytoscape: a software environment for integrated models of biomolecular interaction networks. *Genome Res.* 13:2498–2504. <https://doi.org/10.1101/gr.1239303>
- Silva, M., N. Morsci, K.C.Q. Nguyen, A. Rizvi, C. Rongo, D.H. Hall, and M.M. Barr. 2017. Cell-Specific  $\alpha$ -Tubulin Isoform Regulates Ciliary Microtubule Ultrastructure, Intraflagellar Transport, and Extracellular Vesicle Biology. *Curr. Biol.* 27:968–980. <https://doi.org/10.1016/j.cub.2017.02.039>
- Sirajuddin, M., L.M. Rice, and R.D. Vale. 2014. Regulation of microtubule motors by tubulin isotypes and post-translational modifications. *Nat. Cell Biol.* 16:335–344. <https://doi.org/10.1038/ncb2920>
- Straight, A.F., W.F. Marshall, J.W. Sedat, and A.W. Murray. 1997. Mitosis in living budding yeast: anaphase A but no metaphase plate. *Science.* 277:574–578. <https://doi.org/10.1126/science.277.5325.574>
- Sturgill, E.G., and R. Ohi. 2013. Microtubule-regulating kinesins. *Curr. Biol.* 23:R946–R948. <https://doi.org/10.1016/j.cub.2013.08.012>
- Theurkauf, W.E., H. Baum, J. Bo, and P.C. Wensink. 1986. Tissue-specific and constitutive alpha-tubulin genes of *Drosophila melanogaster* code for structurally distinct proteins. *Proc. Natl. Acad. Sci. USA.* 83:8477–8481. <https://doi.org/10.1073/pnas.83.22.8477>
- Ti, S.-C., G.M. Alushin, and T.M. Kapoor. 2018. Human  $\beta$ -Tubulin Isoforms Can Regulate Microtubule Protofilament Number and Stability. *Dev. Cell.* 47:175–190.e5. <https://doi.org/10.1016/j.devcel.2018.08.014>
- Toda, T., Y. Adachi, Y. Hiraoka, and M. Yanagida. 1984. Identification of the pleiotropic cell division cycle gene NDA2 as one of two different  $\alpha$ -tubulin genes in *Schizosaccharomyces pombe*. *Cell.* 37:233–242. [https://doi.org/10.1016/0092-8674\(84\)90319-2](https://doi.org/10.1016/0092-8674(84)90319-2)
- Usaj, M., Y. Tan, W. Wang, B. VanderSluis, A. Zou, C.L. Myers, M. Costanzo, B. Andrews, and C. Boone. 2017. TheCellMap.org: A Web-Accessible Database for Visualizing and Mining the Global Yeast Genetic Interaction Network. *G3 (Bethesda).* 7:1539–1549. <https://doi.org/10.1534/g3.117.040220>
- Vemu, A., J. Atherton, J.O. Spector, A. Szyk, C.A. Moores, and A. Roll-Mecak. 2016. Structure and Dynamics of Single-isoform Recombinant Neuronal Human Tubulin. *J. Biol. Chem.* 291:12907–12915. <https://doi.org/10.1074/jbc.C116.731133>
- Vemu, A., J. Atherton, J.O. Spector, C.A. Moores, and A. Roll-Mecak. 2017. Tubulin isoform composition tunes microtubule dynamics. *Mol. Biol. Cell.* 28:3564–3572. <https://doi.org/10.1091/mbc.e17-02-0124>
- Weinstein, B., and F. Solomon. 1990. Phenotypic consequences of tubulin overproduction in *Saccharomyces cerevisiae*: differences between alpha-tubulin and beta-tubulin. *Mol. Cell. Biol.* 10:5295–5304. <https://doi.org/10.1128/MCB.10.10.5295>
- Yin, H., D. Pruyne, T.C. Huffaker, and A. Bretscher. 2000. Myosin V orientates the mitotic spindle in yeast. *Nature.* 406:1013–1015. <https://doi.org/10.1038/35023024>
- Zheng, C., M. Diaz-Cuadros, K.C.Q. Nguyen, D.H. Hall, and M. Chalfie. 2017. Distinct effects of tubulin isotype mutations on neurite growth in *Caenorhabditis elegans*. *Mol. Biol. Cell.* 28:2786–2801. <https://doi.org/10.1091/mbc.e17-06-0424>

Supplemental material

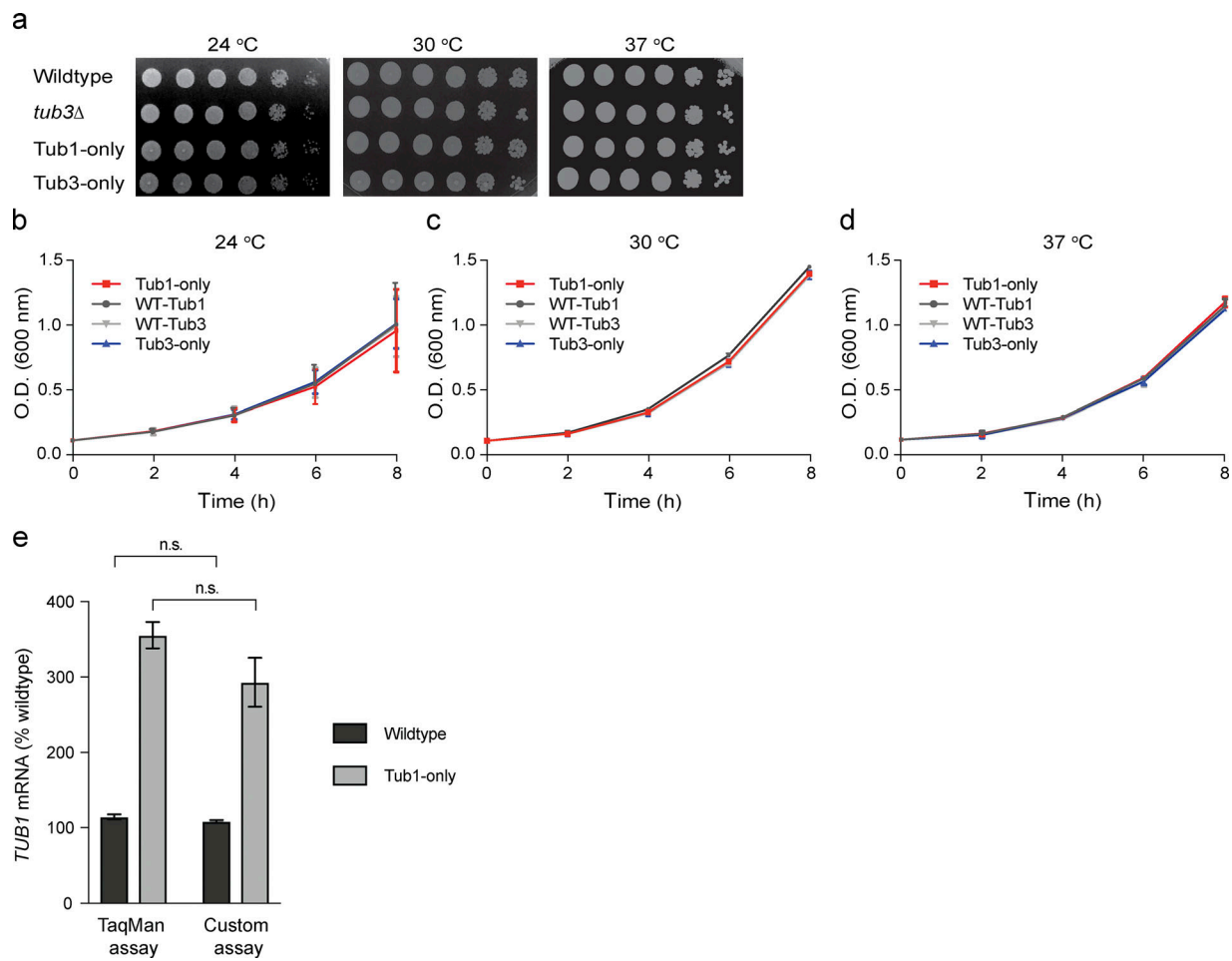


Figure S1. **Growth rate of single isotype strains and *TUB1* mRNA transcript levels measured by the predesigned TaqMan or custom assays.** **(a)** Spotting growth assay. Log-phase cultures of the indicated cell type were serially diluted (fivefold), spotted onto rich media, and incubated at the indicated temperature for 3 d. **(b–d)** Growth rate of the indicated cell types in liquid media at 24°C (b), 30°C (c), and 37°C (d). Graphs represent mean ± SEM from two trials. **(e)** *TUB1* mRNA levels in WT (black) and Tub1-only (gray) cells using either the predesigned TaqMan assay (Thermo Fisher Scientific) or a custom probe/primers assay. The experiment was repeated four times with the TaqMan assay and twice with the custom assay. Each repetition was performed with an independent culture and RNA/cDNA preparation. Results are shown as mean ± SEM; n.s., not significant by unpaired, two-tailed Student's *t* test.

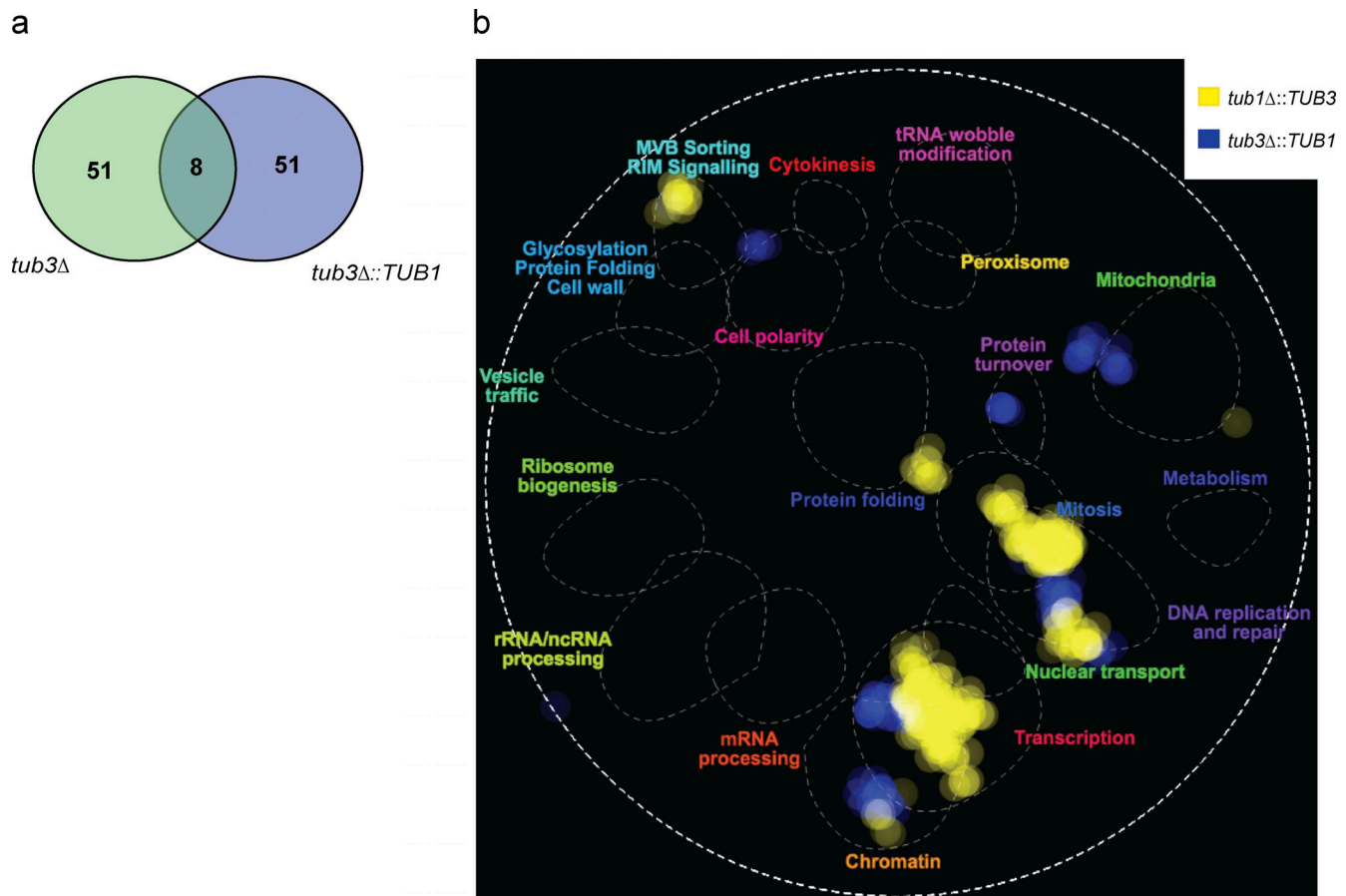


Figure S2. **Genetic interactions for *TUB1* and *TUB3*.** (a) Venn diagram of negative synthetic genetic interactions identified in our loss of *TUB3* (blue; *tub3Δ::TUB1*) SGA screen and nonessential genes reported for simple *TUB3* deletion (green; *tub3Δ*) SGA (Costanzo et al. 2016). Both screens identified 59 stringent interactions, with 8 hits common between both screens. (b) CellMap diagram showing negative synthetic genetic interaction networks with associated GO-term categories for the loss of *TUB1* (yellow; *tub1Δ::TUB3*) or *TUB3* (blue; *tub3Δ::TUB1*; Usaj et al., 2017). MVB, multivesicular body pathway (involved in ubiquitin-dependent sorting into endosomes and lysosome); RIM, regulator of IME2 pathway (involved in cell wall synthesis, meiosis, spore formation).



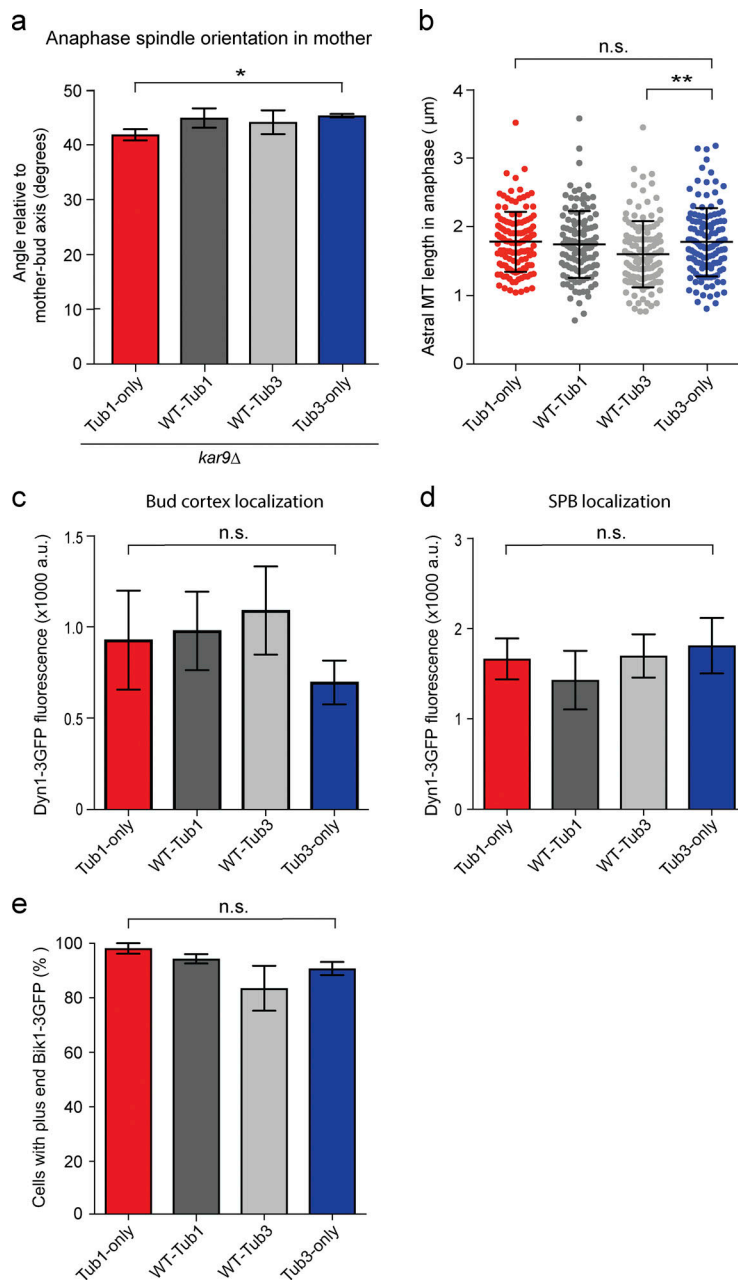
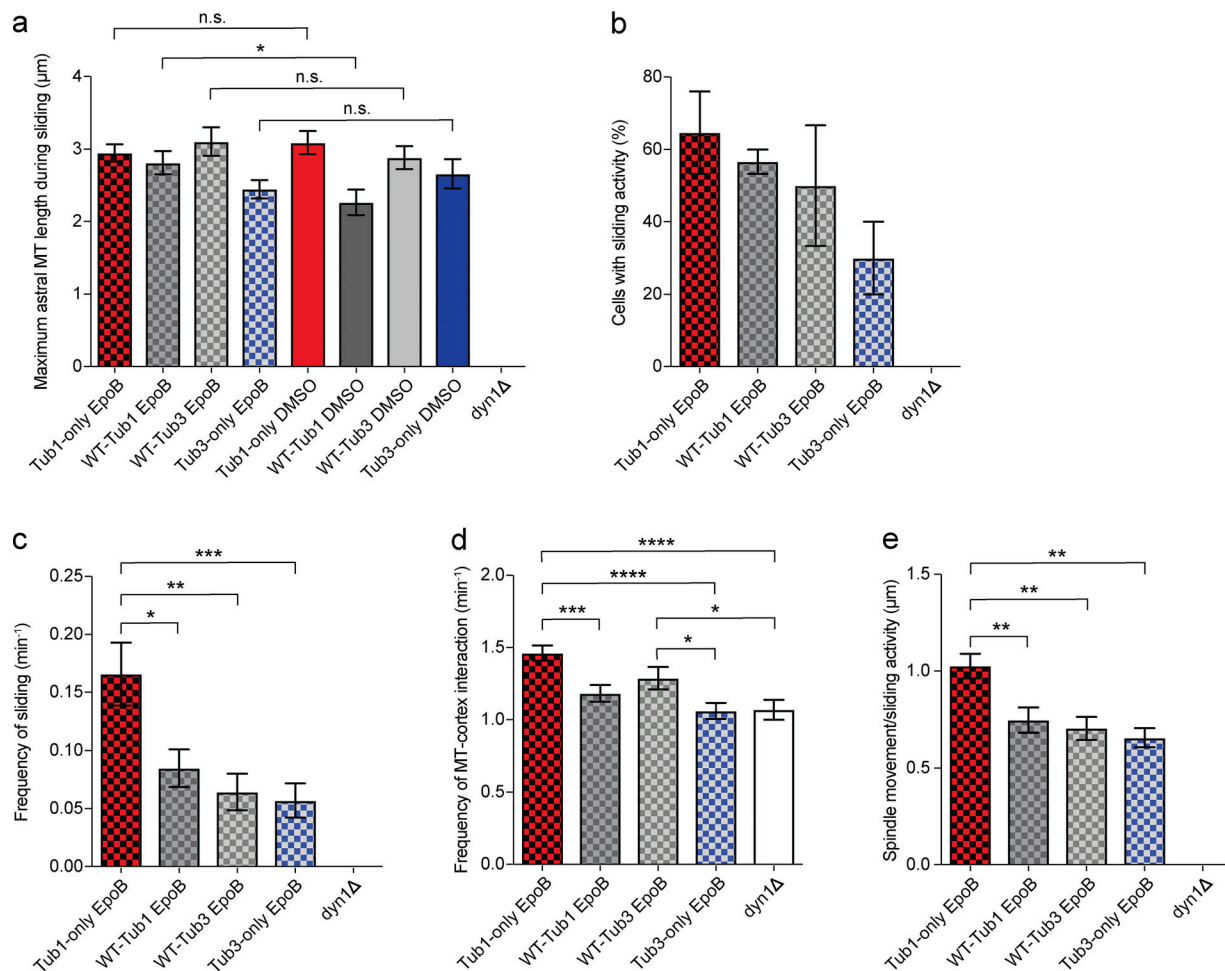


Figure S3. **Anaphase spindle orientation, Dynein localization at the bud cortex and SPB, and the proportion of cells with plus end foci of Bik1.** **(a)** Orientation of anaphase spindle in mother cell of *kar9Δ* cells with the indicated tubulin genotype. **(b)** Length of astral microtubules during anaphase. **(c and d)** Dyn1-3GFP fluorescence intensity at the bud cell cortex (c) and daughter-bound SPB (d) in the indicated cell types. **(e)** Percentage of cells with visible Bik1-3GFP foci at astral microtubule plus ends. Each panel shows mean  $\pm$  SEM from three trials; in panel a, for Tub1 only,  $n = 20, 20,$  and  $21$ ; for WT-Tub1,  $n = 20, 23,$  and  $23$ ; for WT-Tub3,  $n = 20, 20,$  and  $19$ ; for Tub3 only,  $n = 20, 20,$  and  $21$ . In panel b, plot shows microtubules observed from three trials with a total of  $128, 124, 126,$  and  $127$  for Tub1 only, WT-Tub1, WT-Tub3, and Tub3 only, respectively. In panel c, for Tub1 only,  $n = 14, 17,$  and  $16$ ; for WT-Tub1,  $n = 12, 12,$  and  $9$ ; for WT-Tub3,  $n = 9, 11,$  and  $11$ ; for Tub3 only,  $n = 4, 15,$  and  $17$ . In panel d, for Tub1 only,  $n = 34, 33,$  and  $28$ ; for WT-Tub1,  $n = 29, 30,$  and  $33$ ; for WT-Tub3,  $n = 42, 34,$  and  $31$ ; for Tub3 only,  $n = 30, 30,$  and  $35$ . In panel e, for Tub1 only,  $n = 65, 62,$  and  $63$ ; for WT-Tub1,  $n = 73, 61,$  and  $76$ ; for WT-Tub3,  $n = 67, 63,$  and  $70$ ; for Tub3 only,  $n = 68, 63,$  and  $81$ . \*,  $P \leq 0.05$ ; \*\*,  $P \leq 0.01$ ; n.s., not significant for Tub1 only versus Tub3 only ( $P = 0.94$  in panel b,  $P = 0.479$  in panel c,  $P = 0.721$  in panel d, and  $P = 0.075$  in panel e) using the unpaired, two-tailed Student's  $t$  test. MT, microtubule.



**Figure S4. Dynein pathway function is enhanced in Tub1-only versus Tub3-only cells with epothilone-stabilized microtubules.** Drug-sensitized cells (*pdr1Δ pdr3Δ*) in mid-log phase were arrested in HU for 90 min, followed by addition of 10 μM epothilone B (EpoB) for another 60 min (a–e). Parameters of Dynein-mediated sliding activity in epothilone B- or mock (DMSO)-treated cells of the indicated genotypes. Note: Dynein deletion cells (far right; *dyn1Δ*) are not drug sensitized and were not treated with epothilone B or DMSO. Absence of a bar indicates no events were observed in *dyn1Δ* cells. **(a)** Maximum length attained by astral microtubules during Dynein-mediated spindle sliding. Maximum length during sliding is generally comparable in mock and epothilone B-treated cells. **(b)** Percentage of cells that display Dynein-mediated spindle sliding movements. **(c)** Frequency of Dynein-mediated spindle sliding movements in individual cells. **(d)** Frequency of astral microtubule contact with the bud cell cortex in individual cells. **(e)** Distance of spindle translocation by Dynein-mediated sliding events. For panels a–e, graphs show mean ± SEM from two trials; 30–40 cells were analyzed per genotype for each treatment condition; for Dynein-mediated sliding events, in Tub1-only epothilone B, *n* = 12 and 43; WT-Tub1 epothilone B, *n* = 13 and 12; WT-Tub3 epothilone B, *n* = 5 and 14; Tub3-only epothilone B, *n* = 6 and 16; Tub1-only DMSO, *n* = 27 and 19; WT-Tub1 DMSO, *n* = 8 and 13; WT-Tub3 DMSO, *n* = 12 and 10; and Tub3-only DMSO, *n* = 6 and 12. For *dyn1Δ* cells, *n* = 0 and 0 for observed sliding events. n.s., not significant; \*, *P* ≤ 0.05; \*\*, *P* ≤ 0.01; \*\*\*, *P* ≤ 0.001; \*\*\*\*, *P* ≤ 0.0001 by unpaired, two-tailed Student's *t* test. MT, microtubule.

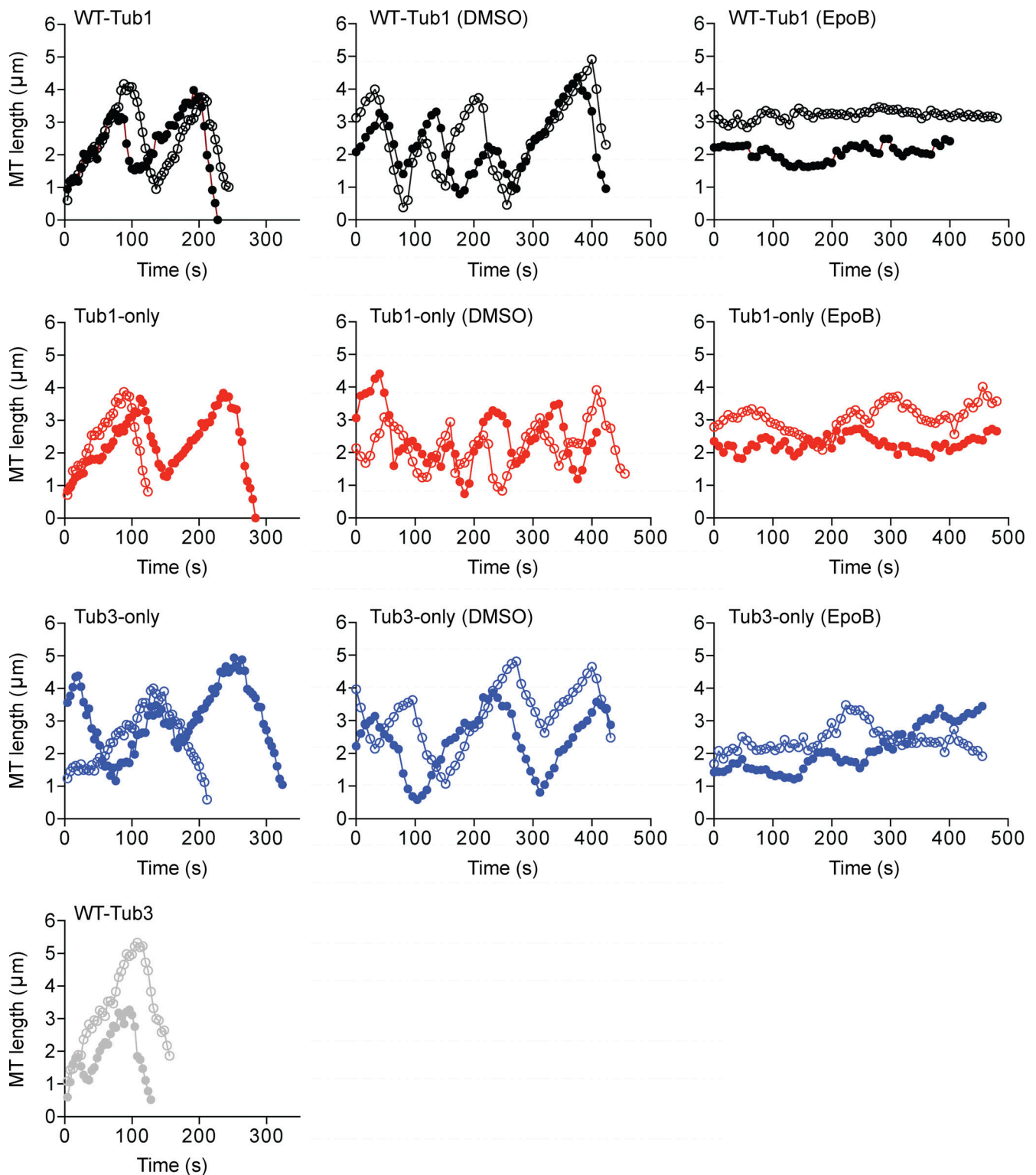


Figure S5. **Representative lifetime history plots of astral microtubules in HU-arrested, mock-treated, and epothilone-treated cells.** Epothilone treatment significantly stabilizes microtubules in WT, Tub1-only, and Tub3-only cells. Two microtubules are shown for each of the indicated cell types in untreated (left), mock (DMSO; middle), and 10  $\mu\text{M}$  epothilone B treatment (EpoB; right). Tub1-only cells contain the *TUB1* ORF in both the *TUB1* and *TUB3* loci, while Tub3-only cells harbor the *TUB3* ORF in both. Microtubules in Tub1-only and Tub3-only cells were visualized with an exogenous copy of GFP-Tub1 and GFP-Tub3, respectively. WT-Tub1 and WT-Tub3 are WT cells harboring an exogenous copy GFP-Tub1 and GFP-Tub3, respectively. MT, microtubule.

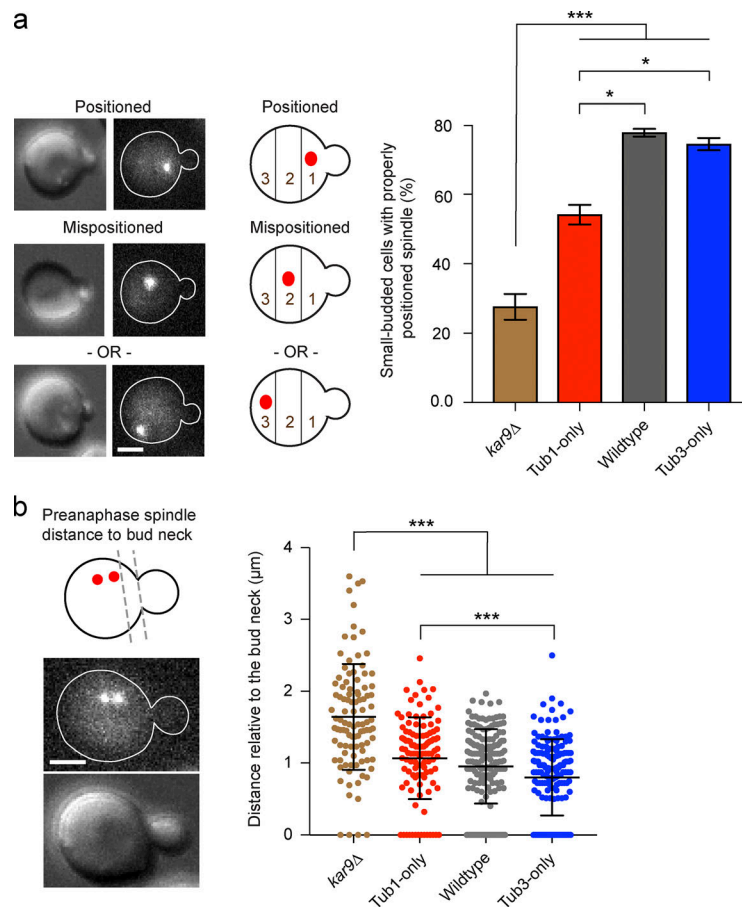


Figure S6. **Tub3 optimizes Kar9-dependent spindle positioning as observed in cells expressing nontagged tubulins solely from the two endogenous loci.** Spindle positioning was monitored by visualizing SPBs (yeast spindle poles) with fluorescently tagged Cnm67-mRUBY2. **(a)** Number of small-budded cells of the indicated genotype with properly positioned early mitotic spindles (category 1 on left). Micrographs show cell (far left) and Cnm67-mRUBY2 image with cell outline in white (second from left) that are representative of categories shown in cartoons. Early mitotic spindles were classified as small-budded cells with duplicated but unseparated SPBs. **(b)** Preanaphase spindle position relative to the bud neck. Micrographs under cartoon show representative cell (lower) and Cnm67-mRUBY2 image with cell outline in white (upper). For panel a, bars show mean  $\pm$  SEM from two trials; for *kar9Δ*,  $n = 67$  and 92; Tub1 only,  $n = 86$  and 40; WT,  $n = 118$  and 132; and Tub3 only,  $n = 120$  and 90. For panel b, line and error bars represent mean  $\pm$  SEM, and scatterplot shows individual cells observed in two trials with a total of 101, 111, 175, and 167 for *kar9Δ*, Tub1 only, WT, and Tub3 only, respectively. \*,  $P \leq 0.05$ ; \*\*\*,  $P \leq 0.001$  by unpaired, two-tailed Student's *t* test. Scale bars = 2  $\mu\text{m}$ .

Video 1. **Time-lapse images of Dynein-mediated mitotic spindle sliding in a HU-arrested (S-phase) control cell with microtubules labeled with GFP-Tub1 and their plus ends enhanced with Bik1-3GFP.** Images were captured at 8-s intervals and represent composite maximum projections of seven z-planes spaced 0.75  $\mu\text{m}$  apart. Video plays at 8 fps and encompasses 2.5 min.

Video 2. **Time-lapse images of dynamic astral microtubules in a HU-arrested (S-phase) WT (WT-Tub1) cell with microtubules labeled with GFP-Tub1 and their plus ends enhanced with Bik1-3GFP.** Images were captured at 4-s intervals and represent composite maximum projections of seven z-planes spaced 0.75  $\mu\text{m}$  apart. Video plays at 10 fps and encompasses 5.4 min.

Video 3. **Time-lapse images of dynamic astral microtubules in a HU-arrested (S-phase) Tub1-only cell with microtubules labeled with GFP-Tub1 and their plus ends enhanced with Bik1-3GFP.** Images were captured at 4-s intervals and represent composite maximum projections of seven z-planes spaced 0.75  $\mu\text{m}$  apart. Video plays at 10 fps and encompasses 4.8 min.

Video 4. **Time-lapse images of dynamic astral microtubules in a HU-arrested (S-phase) Tub3-only cell with microtubules labeled with GFP-Tub1 and their plus ends enhanced with Bik1-3GFP.** Images were captured at 4-s intervals and represent composite maximum projections of seven z-planes spaced 0.75  $\mu\text{m}$  apart. Video plays at 10 fps and encompasses 5 min.

Video 5. **Time-lapse images of dynamic astral microtubules in a mock-treated (DMSO) HU-arrested (S-phase) Tub3-only cell with microtubules labeled with GFP-Tub1 and their plus ends enhanced with Bik1-3GFP.** Images were captured at 8-s intervals and represent composite maximum projections of 10 z-planes spaced 0.75  $\mu\text{m}$  apart. Video plays at 10 fps and encompasses 9.3 min.

Video 6. **Time-lapse images of dynamic astral microtubules in an epothilone B-treated (EpoB) HU-arrested (S-phase) Tub3-only cell with microtubules labeled with GFP-Tub1 and their plus ends enhanced with Bik1-3GFP.** Images were captured at 8-s intervals and represent composite maximum projections of 10 z-planes spaced 0.75  $\mu\text{m}$  apart. Video plays at 10 fps and encompasses 5.1 min.

**Table S1 and Table S2 are provided online as separate files. Table S1 lists the *TUB1* and *TUB3* SGA dataset. Table S2 lists yeast strains and plasmids used in this study.**